Concurrent shape optimization of the part and scanning path for additive manufacturing

Mathilde Boissier, Grégoire Allaire, Christophe Tournier

CONCURRENT SHAPE OPTIMIZATION OF THE PART AND SCANNING PATH FOR ADDITIVE MANUFACTURING

M. BOISSIER[1,2*], G. ALLAIRE[1], C. TOURNIER[2]

[1] *CMAP, École Polytechnique, CNRS UMR7641, Institut Polytechnique de Paris, Palaiseau, France*
[2] *Université Paris-Saclay, ENS Paris-Saclay, LURPA, 91190 Gif-sur-Yvette, France*

[*] *mathilde.boissier@polytechnique.edu*

Abstract: This paper investigates concurrent path planning optimization and built part's structure optimization for powder bed fusion additive manufacturing processes. The state of the art mainly studies trajectories based on existing patterns and, besides their mechanical evaluation, their relevance has not been related to the object's shape. In this work a steady state model of the process is first proposed. Then a systematic path optimization approach free from a priori restrictions and classic structural optimization tools both based on shape optimization theory are combined. This multiphysics optimization leads to innovative and promising results. Not only they confirm that it is essential to take into account the part's shape within the scanning path optimization but they also give hints to some design recipes: the material and the source parameters must be related to the thickness of the bars that compose the structure. Indeed, this thickness is essential to characterize the ability to scan the bar as well as efficient path patterns to do so: straight line, Omega-pattern and Wave-pattern.

Keywords. Path planning and control, additive manufacturing, metallic powder bed fusion, structural optimization.

CONTENTS

1 Introduction

Among the several existing additive manufacturing (AM) processes [1], this work focuses on powder bed fusion (PBF) [2, 3, 4, 5]. This method consists in building metallic parts layer by layer: for each layer, metallic powder is regularly distributed on the top of the already built part. A heat source (laser or electron beam) is then travelled along a prescribed path, melting the powder in specific area. Finally, the part solidifies while cooling down and a new layer of powder is coated to repeat the process. This technology presents several advantages [1, 6]: for example, they modify and reduce traditional building constraints and thus allow for manufacturing complex parts closer to optimal designs, they cut loose with mass production, etc.
These assets make any technological improvement crucial. Among the existing issues, the quality of the final structure must be controlled and improved. While manufacturing each layer, several phenomena (mechanical, metallurgical, thermal) are involved. Ill controlled, they can result in quality defects such as porosity, introduction of residual stresses, rough surfaces or anisotropy [2, 3, 7]. A high fidelity characterization of these defects

must take into account four metal states (powder, solid, fluid, gas) and thus non linear equations making the computations very expensive [2, 8, 9]. Simplified models have thus been set [10] and specific parameters identified to increase the final structure's quality [7, 11]. Moreover, this issue can also be dealt with resorting to post treatments [2, 3]. A second issue affects the building time: any efficiency gain at a layer scale results in a significant manufacturing time reduction.

Among the several manufacturing parameters that can be focused on, it has been chosen in this work to improve the scanning path along which the heat source travels together with the design of the part to build. Indeed, not only it is possible to improve the scanning path used but also the efficiency and quality constraints related to this issue can be included in the part's design itself. Then, following the works already initiated in additive manufacturing in the context of supports [12, 13, 14], the part's shape and topology could be a tool to absorb manufacturing issues allowing the user to compromise between the optimality of the part's structure and the efficiency of the building process.

In automated production, improving the path is a classic issue. Already considered for traditional machining such as milling or welding [15, 16, 17, 18], this path for powder bed fusion technologies directly impacts the heat distribution and thus both the scanning time [19, 20] and the introduction of quality defects [21, 22, 23]. Departing from the literature (see [24] for a review of the existing strategies), where paths are based upon fixed strategies which choice does not involve the part shape, it is chosen here to consider a systematic optimization approach detailed in [25] and with further details in [26]. In this approach, the path is optimized without a priori fixed strategy and is thus expected to be evolving when applied to different part shapes. A focus on temperature control is chosen at the cost of accurate mechanical computations. This allows for the development of path optimization algorithms under a steady state assumption as well as in a more general transient context. This type of systematic optimization of the scanning path is recent with only a limited literature: the work detailed in [27, 28] must be mentioned focusing on an optimal control method with theoretical results; the work initiated by [29] on anisotropy and further developed with [30, 31] models the scanning path connected components as the level sets of a function controlling the residual stresses using an inherent strain method and under a steady state modeling assumption. One originality of the work presented here is that the part's structure is also at stake since its shape and topology is optimized, concurrently with the scanning path.

In this article, the work initiated in [25] under a steady state modeling assumption is carried on to develop a concurrent optimization algorithm aimed at determining both the scanning path and part's structure: the numerical results point out interesting relations between path and part's shape (including its topology) and hint towards promising perspectives to integrate scanning path issues in the part's design.

In Section 2, the model elaborated for this study is presented. This problem is multiphysics: a mechanical problem of compliance minimization under fixed volume constraint is set concerning the final use of the part, and a thermal problem, modeled under a steady state assumption, is defined for the scanning path issues. The scanning path being included in each layer's plane, the model is limited to one layer only and given in two space dimensions. The optimization objectives and constraints resulting from each physics are detailed leading to the definition of the concurrent optimization problem.

For efficiency reasons, it has been chosen here to work with gradient-descent based algorithms. This requires the determination of gradients related to the optimization problem. For both the path and the part's structure optimization, shape optimization tools are used. Section 3 details the derivatives computations with respect to the path and to the part's shape and topology as well as the process to transform them into gradients.

Section 4 details the numerical choices. Since the optimization problem, derivatives and gradients are defined in a continuous setting, Section 4 describes their numerical implementation. In particular, the numerical representations of path and shape, their impact on the optimization problem and gradients definition and the proposed solution algorithm are presented.

Section 5 finally illustrates the optimization process with numerical results. With two mechanical test cases (small cantilever and large cantilever) and two physical test cases (with the metal considered being successively aluminium and titanium), a diversity of results is given. This leads to several observations and thus gives some conclusions.

2 Modelling and optimization problem

In this work, both the part to build and the associated scanning path are simultaneously optimized in the powder bed fusion context. Beforehand, a model of this process must be set and an optimization problem defined. The focus is in this work on a single layer and thus on a two dimensional problem. In this layer, the part shape is actually a two dimensional section of the 3-d part to build and the path is chosen to melt this part shape in the layer (Figure 1). The working or computational domain $D \subset \mathbb{R}^2$ is the cross-section of the build chamber containing this layer, thus a rectangle in practice. In this section, the mechanical problem related to the part optimization is first described before setting the building process model to include path issues.

2.1 Mechanical problem governing the part optimization

Before being manufactured, the part to build is designed for a specific use. In this work, for a linearized elasticity model, the part's compliance is minimized under a volume constraint.

Let $\mathcal{U}_\Omega$ be the space of admissible shapes $\Omega \subset D$ which are open bounded sets with smooth boundary, $\partial\Omega$, composed of three disjoints parts (Figure 1): $\partial\Omega_N$ on which a load $h \in L^2(\partial\Omega_N)^2$ is applied (Neumann boundary condition), $\partial\Omega_D$ on which the elastic displacement is prescribed (Dirichlet boundary condition) and $\partial\Omega_F$ which is traction-free. Only the boundary $\partial\Omega_F$ is optimized and the boundary $\partial\Omega_D$ is assumed to be not empty. The normal of the boundary pointing outward the set Ω is denoted n_Ω. The solid (and corresponding shape Ω) is comprised of an elastic material with a Hooke's tensor A relating the elastic stress and strain defined such that, for any symmetric matrix ξ,

$$A\xi = \left(\frac{E}{1+\nu}\right)\xi + \left(\frac{E\nu}{(1+\nu)(1-2\nu)}\right)\mathrm{Tr}(\xi)I_2, \tag{1}$$

with E the Young modulus and ν the Poisson ratio.The elastic displacement u is solution to the linear elasticity system

$$\begin{cases} -\mathrm{div}\,(A\varepsilon(u)) = 0 & \text{in } \Omega \\ A\varepsilon(u).n_\Omega = h & \text{on } \partial\Omega_N \\ A\varepsilon(u).n_\Omega = 0 & \text{on } \partial\Omega_F \\ u = 0 & \text{on } \partial\Omega_D, \end{cases} \tag{2}$$

where

$$\varepsilon(u) = \frac{1}{2}\left(\nabla u + \nabla u^T\right).$$

Setting

$$H^1_D(\Omega,\mathbb{R}^2) = \{v \in H^1(\Omega,\mathbb{R}^2), \text{ such that } v = 0 \text{ on } \partial\Omega_D\}, \tag{3}$$

the set of functions in $H^1(\Omega,\mathbb{R}^2)$ vanishing on $\partial\Omega_D$, the variational formulation of (2) is to find $u \in H^1_D(\Omega,\mathbb{R}^2)$ such that

$$\int_\Omega A\varepsilon(u) : \varepsilon(\varphi)dx - \int_{\partial\Omega_N} h\cdot\varphi ds = 0, \qquad \forall\varphi \in H^1_D(\Omega,\mathbb{R}^2). \tag{4}$$

The optimization problem consists in minimizing the compliance

$$\min_{\Omega\in\mathcal{U}_\Omega} C_{\mathrm{ply}}(\Omega) = \int_\Omega A\varepsilon(u) : \varepsilon(u)dx$$

under a given volume constraint $V = \int_\Omega dx = V^{\mathrm{target}}$.

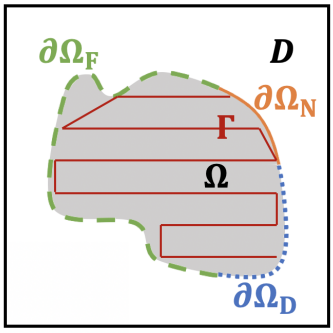

Figure 1: Layer plane: Ω part to build and Γ scanning path

2.2 Problem governing the path feasibility

To include the building considerations, we rely on a simplified model to simulate the process. Indeed, an accurate description of the process (taking into account all phase changes, metallurgical and mechanical aspects) would require a too complicated and CPU expensive model for optimization purposes. Therefore, the focus is rather on a simplified macro-scale model [2, 8] that involves a thermal problem only. In this context, the control on the fabrication of the part, as well as on the appearance of residual stresses [32], is performed solely

through the temperature. Adding the hypothesis of an infinite scanning speed, the model is further simplified by getting rid of the time dependence of the problem. Note that some of the heat sources used in the powder bed fusion context (and especially electron beams) can move very fast along the path: if the steady state property of our model is obviously a restrictive assumption, the results can nevertheless be physically interpreted. For further information on how to derive such a model, on its advantages and on its limits, the interested reader is referred to [26, 25].

Let $\mathcal{U}_\Gamma$ be the space of admissible paths Γ which are $\mathcal{C}^2$ oriented curves such that $\Gamma \subset D$, with tangent τ_Γ, starting at some point A and ending at point B (depending on Γ). The normal n_Γ is defined such that, $\forall x \in \Gamma$, $(\tau_\Gamma(x), n_\Gamma(x))$ is a direct orthonormal basis. The (mean) curvature is given at each point by $\kappa_\Gamma(x) = \mathrm{div}(n_\Gamma(x))$ where the normal has been extended to a neighborhood of Γ. Note that this curvature is well defined since the curves $\Gamma \in \mathcal{U}_\Gamma$ are $\mathcal{C}^2$. In the following, it is assumed that the path is switched on at once leading to the following heat equation:

$$\begin{cases} -\nabla(\lambda \nabla y) + \beta(y - y_{\mathrm{ini}}) = P\chi_\Gamma & \text{in } D, \\ \lambda \partial_n y = 0 & \text{on } \partial D. \end{cases} \tag{5}$$

with λ the conductivity, P the constant source power, Γ the scanning path and $\chi_\Gamma(x)$ the Dirac function supported by the path. This heat equation models the conduction effects in the layer plane as well as in the building direction, through the introduction of a temperature loss term with coefficient β. The variational formulation of (5) consists in finding $y \in H^1(D)$ such that

$$\int_D (\lambda \nabla y \cdot \nabla \phi + \beta(y - y_{\mathrm{ini}})\phi)\, dx = \int_\Gamma P\phi ds, \qquad \forall \phi \in H^1(D). \tag{6}$$

Controlling the feasibility of the part with respect to the path Γ is monitored by three different constraints which should vanish:

- Control of the solid region. The part $\Omega \subset D$ must solidify (Figure 1). Thus, at each point $x \in \Omega$, the temperature, y, must be above a change of state temperature y_ϕ, namely $y(x) \geq y_\phi$. Therefore, with $(.)^+ = \max(.,0)$, this pointwise constraint can be translated into only one constraint, referred to as "phase constraint" in the following,

$$C_\phi = \int_\Omega \left[\left(y_\phi - y(x) \right)^+ \right]^2 dx. \tag{7}$$

- Control of the powder region. The part $D \setminus \Omega$ must remain powder. Thus, at each point $x \in D \setminus \Omega$, the temperature, y, must remain under a maximum temperature $y_{M,D\setminus\Omega} \leq y_\phi$, namely $y(x) \leq y_{M,D\setminus\Omega}$. A constraint, referred to as "maximum temperature constraint out of the part" in the following, can then be introduced

$$C_{M,D\setminus\Omega} = \int_{D\setminus\Omega} \left[\left(y(x) - y_{M,D\setminus\Omega} \right)^+ \right]^2 dx. \tag{8}$$

- Control of the defects. To avoid the appearance of defects in the part during its building (especially residual stresses and deformations), the maximum temperature is required to stay below a fixed threshold. Thus, at each point $x \in \Omega$, the temperature y must remain below a maximum temperature $y_{M,\Omega}$, namely $y(x) \leq y_{M,\Omega}$. The choice of the maximal temperature $y_{M,\Omega}$ is somehow arbitrary and obviously impacts the optimization results. For further details, the reader can refer to [26] and especially to Chapter 6. The "maximum temperature constraint in the part" is the defined by

$$C_{M,\Omega} = \int_\Omega \left[\left(y(x) - y_{M,\Omega} \right)^+ \right]^2 dx. \tag{9}$$

The optimization problem is to minimize the path length

$$\min_{\Gamma \in \mathcal{U}_\Gamma} L_\Gamma = \int_\Gamma ds,$$

under the constraints that $C_\phi = 0$, $C_{M,D\setminus\Omega} = 0$, $C_{M,\Omega} = 0$.

2.3 Concurrent optimization problem

The concurrent or simultaneous optimization problem gathers both optimization problems of Subsections 2.1 and 2.2. It is a multiphysic problem with two state equations (one mechanical for the final use of the part, one thermal for the building process of the part). It reads

$$\min_{\Omega\in\mathcal{U}_\Omega,\Gamma\in\mathcal{U}_\Gamma} J(\Omega,\Gamma) = l_{\text{cply}}C_{\text{ply}}(\Omega) + l_L L_\Gamma(\Gamma),$$
$$\text{such that } \begin{cases} V(\Omega) = V^{\text{target}}, \\ C(\Omega,\Gamma) = C_\phi(\Omega,\Gamma) + C_{M,\Omega}(\Omega,\Gamma) + C_{M,D\setminus\Omega}(\Omega,\Gamma) = 0, \end{cases} \tag{10}$$

where the various objectives and constraints are computed with the states $u \in H^1(D,\mathbb{R}^2)$, solution of the elasticity equation (2), $y \in H^1(D,\mathbb{R})$, solution of the heat equation (5), and $l_{\text{cply}}, l_L \in \mathbb{R}$ are some weighting coefficients.

Remark 1. *Note that in this work, the path Γ and the shape Ω are independent. This is a modelling choice. To make the problem more complex and more realistic, the shape could be considered dependent on the path Γ. One could also decide to model the shape by the melted zone and thus optimize the path only, the part's shape being completely determined by the path.*

3 Gradient with respect to the path Γ and the shape Ω

The optimization method is based on a gradient descent algorithm. It thus requires the computation of the gradient of each objective and constraint functions with respect to the path Γ and shape Ω. In this work, the shape optimization method is chosen and the gradients computed using the classic method of Céa. The Propositions' proofs are kept simple and the interested reader is referred to [33, 34, 35, 36].

3.1 Differentiation with respect to the shape Ω

Proposition 1 details the differentiation with respect to the shape Ω.

Proposition 1. *Let $\Omega \in \mathcal{U}_\Omega$ and $\Gamma \in \mathcal{U}_\Gamma$. Then, C_{ply}, L_Γ, V and C are differentiable at Ω and for any perturbation $\theta_\Omega \in \mathcal{C}^2(\overline{D},\mathbb{R}^2)$ such that $\forall x \in \partial\Omega_N \cup \partial\Omega_D$, $\theta_\Omega(x) = 0$, their derivatives are*

$$D_\Omega C_{ply}(\Omega)(\theta_\Omega) = \int_{\partial\Omega_F} (-A\varepsilon(u) : \varepsilon(u))\,\theta_\Omega(s)\cdot n_\Omega(s)ds, \tag{11}$$

$$D_\Omega L_\Gamma(\Gamma)(\theta_\Omega) = 0, \tag{12}$$

$$D_\Omega V(\Omega)(\theta_\Omega) = \int_{\partial\Omega_F} \theta_\Omega(s)\cdot n_\Omega(s)ds, \tag{13}$$

and

$$D_\Omega C(\Omega,\Gamma)(\theta_\Omega) = \int_{\partial\Omega_F} \left(\left[\left(y_\phi - y\right)^+ \right]^2 + \left[\left(y - y_{M,\Omega}\right)^+ \right]^2 - \left[\left(y - y_{M,D\setminus\Omega}\right)^+ \right]^2 \right) \theta_\Omega(s)\cdot n_\Omega(s)ds. \tag{14}$$

Remark 2. *Note that, following Hadamard structure theorem [33, 34, 35], for all the considered functions (denoted $G \in \{C_{ply}, L_\Gamma, V, C\}$ in the following), the derivative can be written, with $g_\Omega \in \mathcal{C}^0(\overline{D},\mathbb{R})$.*

$$D_\Omega G(\Omega)(\theta_\Omega) = \int_{\partial\Omega_F} g_\Omega \theta_\Omega \cdot n_\Omega ds. \tag{15}$$

For the proof of Proposition 1 we need the following classical result [33, 34, 35] which is recalled for the sake of completeness.

Lemma 1. *Let $\Omega \subset \mathbb{R}^2$ be a msooth open bounded set. Let $f \in \mathcal{C}^1(D,\mathbb{R})$. The function $J(\Omega) = \int_\Omega f(x)dx$ is differentiable at Ω and $\forall \theta \in \mathcal{C}^2\left(\overline{D},\mathbb{R}^2\right)$,*

$$D_\Omega J(\Omega)(\theta) = \int_{\partial\Omega} f(s)\theta(s)\cdot n_\Omega(s)ds. \tag{16}$$

Proof. First of all, the path does not depend on the shape Ω (see Remark 1) which gives (12). Lemma 1 is then used to compute the derivatives of the compliance, volume and temperature constraint.
Lemma 1 can apply directly for the volume. Since the integrand of the temperature constraint only depends on the temperature and thus on the path and not on the shape, Lemma 1 also apply. Finally, recalling that only the part of boundary $\partial\Omega_F$ is optimizable, the derivatives given by (13) and (14) are finally found.
As for the compliance, the integrand actually depends on the elastic displacement which itself depends on the shape Ω. A differentiation of this displacement with respect to Ω would then be required. To avoid such

computations, the method of Céa [37] is here applied and an extended functional is introduced (recall that $H^1_D(\Omega,\mathbb{R}^2)$ is defined by (3))

$$\mathcal{G}:\left\{\begin{array}{lll}\mathcal{U}_\Omega\times H^1_D(\Omega,\mathbb{R}^2)\times H^1_D(\Omega,\mathbb{R}^2) & \to & \mathbb{R}\\ (\Omega,p,q) & \mapsto & \displaystyle\int_\Omega A\varepsilon(p):\varepsilon(p)+\int_\Omega A\varepsilon(p):\varepsilon(q)dx-\int_{\partial\Omega_N}h\cdot pds.\end{array}\right.$$

Then, $\forall q\in H^1_D(\Omega,\mathbb{R}^2)$, $\mathcal{G}(\Omega,u,q)=C_{\text{ply}}(\Omega)$. Differentiating with respect to the shape Ω then leads to

$$D_\Omega C_{\text{ply}}(\Omega)(\theta)=\partial_\Omega\mathcal{G}(\Omega,u,q)(\theta)+\partial_u\mathcal{G}(\Omega,u,q)\left(\partial_\Omega u(\Omega)(\theta)\right).$$

Choosing $q=u_{\text{adj}}$ such that $\forall\phi\in H^1_D(\Omega,\mathbb{R}^2)$, $\partial_u\mathcal{G}(\Omega,u,u_{\text{adj}})(\phi)=0$ leads to choosing $u_{\text{adj}}\in H^1(\Omega,\mathbb{R}^2)$ solution of

$$\left\{\begin{array}{ll}-\left(A\varepsilon(u_{\text{adj}})\right)=0 & \text{in }\Omega\\ A\varepsilon(u)\cdot n_\Omega=-2h & \text{on }\partial\Omega_N\\ A\varepsilon(u)\cdot n_\Omega=0 & \text{on }\partial\Omega_F\\ u=0 & \text{on }\partial\Omega_D.\end{array}\right.$$

This is equivalent to choosing $u_{\text{adj}}=-2u$. This leads to

$$D_\Omega C_{\text{ply}}(\Omega)(\theta)=\partial_\Omega\mathcal{G}(\Omega,u,-2u)(\theta),$$

and Lemma 1 concludes the proof. □

3.2 Differentiation with respect to the path Γ

Proposition 2 details the differentiation with respect to the path Γ. To compute the derivative, an adjoint function $y_{\text{adj}}\in H^1(D,\mathbb{R})$ is introduced as

$$\left\{\begin{array}{ll}-\nabla\left(\lambda\nabla y_{\text{adj}}\right)+\beta y_{\text{adj}}=2\left[\left(y_\phi-y\right)^+\mathbb{1}_{\Omega_0}-\left(y-y_{M,\Omega}\right)^+\mathbb{1}_{\Omega_0}-\left(y-y_{M,D\setminus\Omega}\right)^+\mathbb{1}_{D\setminus\Omega_0}\right] & \text{in}\,D,\\ \lambda\partial_n y_{\text{adj}}=0 & \text{on}\,\partial D.\end{array}\right.\tag{17}$$

Proposition 2. *Let $\Gamma\in\mathcal{U}_\Gamma$ and $\Omega_0\in\mathcal{U}_\Omega$. Then, C_{ply}, L_Γ, V and C are differentiable at Γ and, for any perturbation $\theta_\Gamma\in\mathcal{C}^2(\overline{D},\mathbb{R}^2)$, their derivatives are as follow:*

$$D_\Gamma C_{ply}(\Omega)(\theta_\Gamma)=0,\tag{18}$$

$$D_\Gamma L_\Gamma(\Gamma)(\theta_\Gamma)=\int_\Gamma\kappa_\Gamma(s)\theta_\Gamma(s)\cdot n_\Gamma(s)ds+\theta_\Gamma(B)\cdot\tau_\Gamma(B)-\theta_\Gamma(A)\cdot\tau_\Gamma(A),\tag{19}$$

$$D_\Gamma V(\Omega)(\theta_\Gamma)=0,\tag{20}$$

and

$$\begin{array}{rl}D_\Gamma C(\Omega_0,\Gamma)(\theta_\Gamma)= & \displaystyle\int_\Gamma\left(-P\left[\partial_n y_{adj}(s)+\kappa_\Gamma(s)y_{adj}(s)\right]\theta_\Gamma(s)\cdot n_\Gamma(s)\right)ds\\ & -Py_{adj}(B)\theta_\Gamma(B)\cdot\tau_\Gamma(B)+Py_{adj}(A)\theta_\Gamma(A)\cdot\tau_\Gamma(A),\end{array}\tag{21}$$

where $y_{adj}\in H^1(D,\mathbb{R})$ is defined by (17).

Remark 3. *Note that, for both the path length and the constraint (denoted $F\in\{C_{ply},L_\Gamma,V,C\}$), following Hadamard structure theorem [33, 34, 35], the derivative can be written*

$$D_\Gamma F(\Gamma)(\theta_\Gamma)=\int_\Gamma f_{n_\Gamma}\theta_\Gamma\cdot n_\Gamma ds+f_{\tau_\Gamma}(B)\theta_\Gamma(B)\cdot\tau_\Gamma(B)-f_{\tau_\Gamma}(A)\theta_\Gamma(A)\cdot\tau_\Gamma(A),\tag{22}$$

with $f_{n_\Gamma},f_{\tau_\Gamma}\in\mathcal{C}^0(\overline{D},\mathbb{R})$.

For the proof of Proposition 2 we need the following classical result [33, 34, 35] which is recalled for the sake of completeness.

Lemma 2. *Let $\Gamma\in\mathcal{U}_\Gamma$, $g\in W^{2,1}(D,\mathbb{R})$. The function $J(\Gamma)=\displaystyle\int_\Gamma g(s)ds$ is differentiable at Γ and $\forall\theta\in\mathcal{C}^2\left(\overline{D},\mathbb{R}^2\right)$,*

$$D_\Gamma J(\Gamma)(\theta)=\int_\Gamma\left(\kappa_\Gamma(s)g(s)+\partial_{n_\Gamma}g(s)\right)\theta(s)\cdot n_\Gamma(s)ds+g(B)\theta(B)\cdot\tau_\Gamma(B)-g(A)\theta(A)\cdot\tau_\Gamma(A).\tag{23}$$

Proof. First of all, the compliance and volume do not depend on the shape Ω (see Remark 1) which give (18) and (20). Lemma 2 is then used to compute the derivatives of the length and temperature constraint.
Lemma 2 can apply directly for the length. As for the temperature constraint, it does not depend explicitly on the path. The dependence is in the temperature, requiring, as for Proposition 1, the use of the method of Céa. The extended functional is

$$\mathcal{G}:\left\{\begin{array}{lll}\mathcal{U}_\Gamma\times H^1(D,\mathbb{R})\times H^1(D,\mathbb{R}) & \to & \mathbb{R}\\ (\Gamma,w,z) & \mapsto & \displaystyle\int_\Omega\left[\left(y_\phi-w\right)^+\right]^2+\left[(w-y_{M,\Omega})^+\right]^2dx+\int_{D\setminus\Omega}\left[\left(w-y_{M,D\setminus\Omega}\right)^+\right]^2\\ & & \displaystyle+\int_D\lambda\nabla w\cdot\nabla z dx-\int_\Gamma Pzds.\end{array}\right.$$

Then, $\forall z\in H^1(\Omega,\mathbb{R}^2)$, $\mathcal{G}(\Gamma,y,z)=C(\Gamma)$. Differentiating with respect to the shape Ω then leads to

$$D_\Gamma C(\Gamma)(\theta)=\partial_\Gamma\mathcal{G}(\Gamma,y,z)(\theta)+\partial_y\mathcal{G}(\Gamma,y,z)\left(\partial_\Gamma y(\Gamma)(\theta)\right).$$

Choosing $z=y_{\text{adj}}$ such that $\forall\phi\in H^1(D,\mathbb{R})$, $\partial_y\mathcal{G}(\Gamma,y,y_{\text{adj}})(\phi)=0$ leads to define $y_{\text{adj}}\in H^1(D,\mathbb{R})$ as the solution of (17). This leads to

$$D_\Gamma C(\Gamma)(\theta)=\partial_\Gamma\mathcal{G}(\Gamma,y,y_{\text{adj}})(\theta),$$

and Lemma 2 concludes the proof. □

3.3 Transformation of the derivative into gradients: regularization-extension process

In order to apply a gradient descent algorithm, a gradient must be deduced from the derivatives given by Propositions 1 and 2. For $X=\Omega$ or $X=\Gamma$, a Hilbert space H_X is chosen together with its scalar product $(.,.)_H$ and the gradient J'_X of a function J corresponds to the Riesz representative of the derivative (which is a linear form) in the Hilbert space.

$$D_XJ(X)(\theta)=(J'_X,\theta)_X. \tag{24}$$

This gradient determination process is classical and can be used as a regularization or regularization-extension process (extension of the shape gradient away from the boundary) [38, 33, 39, 40]. Note that the direction $\theta=-J'_X$ is then a descent direction. Indeed, this leads to $D_XJ(X)(\theta)=-\|J'_X\|_X\leq 0$.

The gradient with respect to the shape is first considered choosing the gradient of each function $G\in\{C_{\text{ply}},L_\Gamma,V,C\}$ as the Riesz representative of the derivative in the Hilbert space $H^1(D,\mathbb{R}^2)$ which amounts to compute $G'=G'_{n_\Omega}n_\Omega\in H^1(D,\mathbb{R}^2)$ such that $\forall Q\in H^1(D,\mathbb{R})$,

$$\int_D\left(\nu_\Omega^2\nabla G'_{n_\Omega}\cdot\nabla Q+G'_{n_\Omega}Q\right)dx=\int_{\partial\Omega_F}g_\Omega Qds. \tag{25}$$

The coefficient $\nu_\Omega>0$ is a regularization coefficient in this "regularization-extension" process.

The Hilbert space $H^1(D;\mathbb{R}^2)$ cannot be used for any curve $\Gamma\in\mathcal{U}_\Gamma$ (available for the shape Ω only), since any function in $H^1(D;\mathbb{R}^2)$ is not necessarily defined at points A and B. Thus, the gradient with respect to the path to each function $F\in\{C_{\text{ply}},L_\Gamma,V,C\}$ is the Riesz representative of the derivative in $H^1(\Gamma,\mathbb{R}^2)$ (Laplace-Beltrami choice) which amounts to compute $F'=F'_{\tau_\Gamma}\tau_\Gamma+F'_{n_\Gamma}n_\Gamma\in H^1(\Gamma,\mathbb{R}^2)$ such that $\forall W=W_{\tau_\Gamma}\tau_\Gamma+W_{n_\Gamma}n_\Gamma$, $W_{\tau_\Gamma},W_{n_\Gamma}\in H^1(\Gamma,\mathbb{R})$,

$$\begin{aligned}D_\Gamma F(\Gamma)(W) &= \int_\Gamma(f_{n_\Gamma}W_{n_\Gamma})\,ds+f_{\tau_\Gamma}(B)W_{\tau_\Gamma}(B)-f_{\tau_\Gamma}(A)W_{\tau_\Gamma}(A),\\ &= \int_\Gamma\left[\nu_\Gamma^2\left(\nabla_{\tau_\Gamma}F'_{\tau_\Gamma}\cdot\nabla_{\tau_\Gamma}W_{\tau_\Gamma}+\nabla_{\tau_\Gamma}F'_{n_\Gamma}\cdot\nabla_{\tau_\Gamma}W_{n_\Gamma}\right)+F'_{\tau_\Gamma}W_{\tau_\Gamma}+F'_{n_\Gamma}W_{n_\Gamma}\right]ds.\end{aligned} \tag{26}$$

This regularization process is controlled by the coefficient $\nu_\Gamma>0$.

4 Numerical algorithm

The optimization method chosen is a double loop algorithm. The outer loop is related to the part shape Ω whereas the inner loop focuses on the path Γ, both of them corresponding to gradient descent algorithms. The number of iterations in each loop determines the balance between the optimization of both variables. The following subsections detail the differentiation process, the discretization and the algorithm related to each loop.

4.1 Inner loop: path optimization

The inner loop focuses on path optimization. Let D be the working domain and Ω_0 a fixed shape that the optimized path must build. The optimization problem related to the inner loop is then

$$\begin{aligned} &\min_{\Gamma \in \mathcal{U}_\Gamma} L_\Gamma(\Gamma), \\ &\text{such that} \quad C = C_\phi(\Omega_0, \Gamma) + C_{M,\Omega}(\Omega_0, \Gamma) + C_{M,D\setminus\Omega}(\Omega_0, \Gamma) = 0, \end{aligned} \tag{27}$$

where $y \in H^1(D, \mathbb{R})$ solution to the heat equation (5). To numerically solve this optimization problem, the strategy is the following: first define a discretization of the problem; and then, choose an optimization algorithm and determine the corresponding numerical gradient from the gradients computed in Subsection 3.2.

4.1.1 Discretization of the optimization problem

Along the inner loop iterations, the path Γ is modified leading to re-evaluations of the temperature y. The numerical representation of each object is crucial since impacting both the computational time and accuracy. Among the several works related to interface representation [41, 42, 43, 44], we follow [45] and choose a front tracking approach. The working domain is discretized with a "(physical) mesh" fixed along the iterations. On this mesh, the finite element functions are defined and the temperature computed. The path is also discretized as a broken line defined by its nodal points $(x_i)_{i\in[\![1,N_x]\!]}$, N_x the number of points. This discretized path (and especially its nodal points) is modified at each iteration (Figure 2). This representation is very convenient because it keeps the mesh fixed, thereby considerably reducing the computational costs. Moreover, the discretized path allows for a full control of the line topology (no uncontrolled changes in the number of connected components).

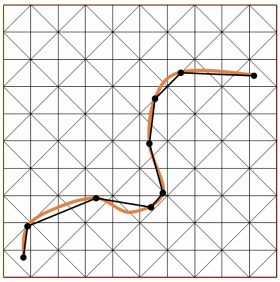

Figure 2: Front-tracking approach: fixed physical mesh and moving broken line path discretization

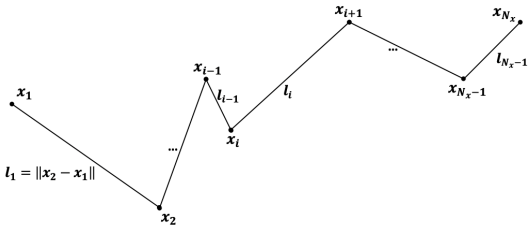

Figure 3: Path description as a broken line

Two technical issues come out of this method [45]. The first one is related to the path description. At each iteration, the path discretization's nodes are advected, modifying the length of each element $(l_i)_{i\in[\![1,N_x-1]\!]}$. To keep a relevant representation, the discretization must be adapted [45, 41]. The resulting line is re-discretized to ensure each segment length to be in the range $[d_{\text{lower}}, d_{\text{upper}}]$. These bounds are chosen so that $d_{\text{upper}} = 2d_{\text{lower}} = 0.7\Delta x$, with Δx the characteristic physical mesh size. During the optimization process, the tangent $(\tau_{\Gamma i})_{i\in[\![1,N_x-1]\!]}$, normal $(n_{\Gamma i})_{i\in[\![1,N_x-1]\!]}$ and curvature $(\kappa_{\Gamma i})_{i\in[\![1,N_x-1]\!]}$ of the line at each nodal point are required (see Proposition 2). The broken line representation of the path implies the definition of discrete tangent, normal and curvature. Their definitions follow [26] Chapter 5, in which all the details of the discretization process can be found. The second issue is related to the information mapping between the discrete path and the physical mesh. Indeed, both meshes hold information that must be shared with each other:

- heat source: the path, defined by its discretization, carries the heat source which must be transformed into a finite element function on the physical mesh: for each cell of the physical mesh, the length of the path is computed and re-normalized to define a $P0-$source function (Figure 4.
- derivative and physical quantities: the gradients of the path length and constraint with respect to the path are determined from physical quantities, defined on the physical mesh and must be transformed into a value at each discrete path nodal point.

Once again, every algorithmic details can be found in [26] Chapter 5.

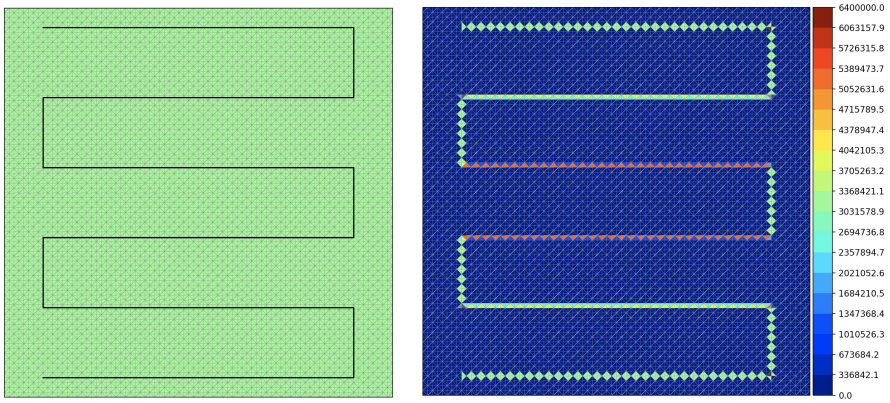

(a) Path Γ carrying the source (b) $P0-$function representing the source

Figure 4: Mapping the source information from the path Γ to the physical mesh

The gradients of the path length and constraint are the solutions of (26) in their continuous version. To get them in a discretized version, compatible with the numerical problem, the gradient equation is discretized. Let F be the function to which the numerical gradient must be computed. Then, $\forall i \in [\![1, N_x]\!]$, its numerical gradient at point x_i, $F'_i = F'_{\tau_\Gamma,i}\tau_{\Gamma i} + F'_{n_\Gamma,i}n_{\Gamma i}$ is such that

$$\begin{cases} \displaystyle\sum_{i=1}^{N_x-1} l_i \left[\nu_\Gamma^2 \left(\frac{F'_{\tau_\Gamma,i+1} - F'_{\tau_\Gamma,i}}{l_i} \frac{W_{i+1} - W_i}{l_i} \right) + \frac{F'_{\tau_\Gamma,i+1} W_{i+1} + F'_{\tau_\Gamma,i} W_i}{2} \right] - f_{\tau_\Gamma,N_x} W_{N_x} + f_{\tau_\Gamma,1} W_1 = 0, \\ \displaystyle\sum_{i=1}^{N_x-1} l_i \left[\nu_\Gamma^2 \left(\frac{F'_{\Gamma,n_\Gamma,i+1} - F'_{\Gamma,n_\Gamma,i}}{l_i} \frac{W_{i+1} - W_i}{l_i} \right) + \frac{F'_{\Gamma,n_\Gamma,i+1} W_{i+1} + F'_{\Gamma,n_\Gamma,i} W_i}{2} - \frac{f_{n_\Gamma,i+1} W_{i+1} + f_{n_\Gamma,i} W_i}{2} \right] = 0. \end{cases} \tag{28}$$

4.1.2 Inner loop optimization algorithm

In order to include the constraint C into the optimization algorithm, an augmented Lagrangian method is chosen [46, 26]. The optimization problem (27) is modified into

$$\max_{l_{C,\Gamma} \in \mathbb{R}} \min_{\Gamma \in \mathcal{U}_\Gamma} \mathcal{L}_\Gamma(\Omega_0, \Gamma, l_{C,\Gamma}, c_{C,\Gamma}) = \frac{L_\Gamma(\Gamma)}{L_\Gamma^0} + l_{C,\Gamma} \frac{C(\Omega_0, \Gamma)}{C^0} + \frac{c_{C,\Gamma}}{2} \left(\frac{C(\Omega_0, \Gamma)}{C^0} \right)^2, \tag{29}$$

with $L_\Gamma^0 = \Gamma^0_{\Omega_0}$ the initial path length and $C^0 = C\left(\Omega_0, \Gamma^0_{\Omega_0}\right)$ the initial constraint. An iterative algorithm is set. At each iteration $k > 0$, the Lagrange multiplier $l_{C,\Gamma}$ and the path nodal points $(x_i)_{i \in [\![1,N_x]\!]}$ are updated reading

$$\begin{cases} l^{k+1}_{C,\Gamma} = l^k_{C,\Gamma} + c_{C,\Gamma} C(\Omega_0, \Gamma^{k+1}_{\Omega_0}), \\ \forall i \in [\![1, N_x]\!],\ x_i^{k+1} = x_i^k - s_\Gamma^k \mathcal{L}'^\Gamma_{\Gamma,i}(\Omega_0, \Gamma^k_{\Omega_0}, l^k_{C,\Gamma}, c_{C,\Gamma}), \end{cases} \tag{30}$$

with $\mathcal{L}'^\Gamma_\Gamma(\Omega_0, \Gamma, l_{C,\Gamma}; c_{C,\Gamma}) = \dfrac{L'^\Gamma_\Gamma}{L^0_\Gamma} + \left(\dfrac{l_{C,\Gamma}}{C^0} + \dfrac{c_{C,\Gamma}}{(C^0)^2} C(\Omega_0 \Gamma) \right) C'^\Gamma(\Omega_0, \Gamma)$. The step s^k_Γ is given by:

$$s^k_\Gamma = \frac{\mathrm{Coef}^k_\Gamma \Delta x}{\max_i(\| \mathcal{L}'^\Gamma_{\Gamma,i}(\Omega_0, \Gamma^k_{\Omega_0}, l^k_{C,\Gamma}, c_{C,\Gamma}) \|)},$$

with Δx the characteristic physical mesh size. The coefficient Coef^k_Γ is initialized to 1 and updated at each iteration so that (line search strategy),

$$\begin{cases} \min(1.2\,\mathrm{Coef}^k_\Gamma, 1), & \mathcal{L}_\Gamma(\Omega_0, \Gamma^{k+1}_{\Omega_0}, l^k_{C,\Gamma}; c_{C,\Gamma}) < \mathrm{tol}^k_\Gamma * \mathcal{L}_\Gamma(\Omega_0, \Gamma^k_{\Omega_0}, l^k_{C,\Gamma}; c_{C,\Gamma}), \\ 0.6\,\mathrm{Coef}^k_\Gamma, & \text{else.} \end{cases} \tag{31}$$

The tolerance is set to $\mathrm{tol}^0_\Gamma = 1$ in the inner loop.

Finally, if some points are outside the domain D, they are orthogonally projected back to D making the algorithm a projected Augmented Lagrangian detailed by Algorithm 1.

the part shape is fixed to Ω_0
$k_\Gamma = 0$, initialization of the path $\Gamma^0_{\Omega_0}$ and multiplier $l^0_{C,\Gamma}$
resolution of the heat equation and computation of the objective function and constraints
computation of the derivatives
while $Coef_\Gamma^{k_\Gamma} \geq 10^{-8}$ *and* $k_\Gamma \leq$ **do**
    update of the tolerance
    path variation such that $\Gamma^{k_\Gamma+1}_{\Omega_0} = \Gamma^{k_\Gamma}_{\Omega_0} - s^{k_\Gamma}_\Gamma \mathcal{L}'_\Gamma(\Omega_0, \Gamma^{k_\Gamma}_{\Omega_0}, l^{k_\Gamma}_{C,\Gamma}; c_{C,\Gamma})$
    re-discretization of the path $\Gamma^{k_\Gamma+1}_{\Omega_0}$
    resolution of the heat equation, computation of the objective function and constraint
    if $\mathcal{L}_\Gamma(\Omega_0, \Gamma^{k_\Gamma+1}_{\Omega_0}, l^{k_\Gamma}_{C,\Gamma}; c_{C,\Gamma}) < \mathcal{L}_\Gamma(\Omega_0, \Gamma^{k_\Gamma}, l^{k_\Gamma}_{C,\Gamma}; c_{C,\Gamma}) * tol^{k_\Gamma}_\Gamma$ **then**
        iteration accepted
        Lagrange multiplier $l_{C,\Gamma}$ updated: $l^{k_\Gamma+1}_{C,\Gamma} = l^{k_\Gamma}_{C,\Gamma} + c_{C,\Gamma} C^{k_\Gamma+1}\left(\Omega_0, \Gamma^{k_\Gamma+1}_{\Omega_0}\right)$
        step increased
        update of the variables
        computation of the derivatives
    end
    else
        iteration rejected
        step decreased
    end
end

Algorithm 1: Inner loop algorithm

Remark 4. *The augmented Lagrangian method is one approach to deal with the constraints, in which their satisfaction is ensured at convergence only. This final convergence may not be reached in a finite (reasonable) number of iterations. In the numerical results, the algorithm has been stopped after a finite number of iterations and the constraint' final value are thus not exactly zero. Improving this constraint's issue is part of the perspectives. Among the different possibilities, a first idea would be to change the chosen algorithm to deal with the constraints. For example, the algorithm developed in [47] could be adapted.*

Remark 5. *Note that each the phase and the maximal temperature constraints are weighted to* 1 *in the constraint C. This choice aimed at simplifying the numerical tests but could be modified: different weights could be chosen or each constraint could be dealt with separately. This could especially be interesting to favour the respect of the part shape in the building. From an industrial point of view, the main objective is to build the part shape and only then to minimize the residual stresses arising.*

4.2 Outer loop: part optimization

The outer loop focuses on part optimization. A descent gradient is set in which at each iteration, the part is first modified before the inner loop algorithm to update the path is applied. The optimization problem corresponding to this outer loop is

$$\begin{aligned} &\min_{\Omega \in \mathcal{U}_\Omega} J(\Omega,\Gamma) = l_{\text{cply}} C_{\text{ply}}(\Omega) + L_\Gamma(\Gamma), \\ &\text{such that } \begin{cases} V(\Omega) = V^{\text{target}}, \\ C(\Omega,\Gamma) = C_\phi(\Omega,\Gamma) + C_{M,\Omega}(\Omega,\Gamma) + C_{M,D\setminus\Omega}(\Omega,\Gamma) = 0, \end{cases} \end{aligned} \tag{32}$$

where $y \in H^1(D,\mathbb{R})$ solution to the heat equation (5) and $u \in H^1(D,\mathbb{R}^2)$ solution to the elasticity equation (2). The strategy to solve this problem is the same than for the path: define a discretization of the problem and then choose an optimization algorithm and determine the corresponding numerical gradients.

4.2.1 Discretization of the optimization problem

Two numerical objects have already been introduced for the inner loop: the discrete path, modified along the optimization process and the physical mesh, fixed (Figure 2). To represent the part shape Ω, a third object is used (Figure 5): the shape is given by the level set of a function ψ defined on the whole working domain D [36, 48] such that

$$\begin{cases} \psi(x) < 0 & x \in \Omega, \\ \psi(x) = 0 & x \in \partial\Omega \cup D, \\ \psi(x) > 0 & x \in D \setminus \overline{\Omega}. \end{cases} \tag{33}$$

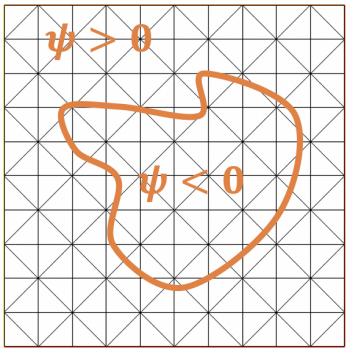

Figure 5: Part numerical representation: fixed physical mesh and part represented by the level set of the function ψ

In this context, the update of the level set is given by the Hamilton Jacobi equation, with t representing the evolution with respect to the iterations and $d_\Omega^{n_\Omega}(t,x)$ the update direction on the normal,

$$\partial_t \psi(t,x) + d_\Omega^{n_\Omega}(t,x)|\nabla\psi(t,x)| = 0, \quad \forall t, \forall x \in D. \tag{34}$$

In numerical applications, the processes described in [49, 50, 51] are used. Along the iterations, the advection equation tends to flatten the level set function values thus "blurring" the results. A re-distanciation algorithm is thus applied based on the signed distance equation [33, 36, 52]. In numerical applications, this function is provided by Freefem++ [53].

4.2.2 Outer loop optimization algorithm

To deal with both the volume and temperature constraints, an augmented Lagrangian method is used, coupled with a dichotomy algorithm on the volume Lagrange multiplier to better satisfy the volume constraint. Introducing the multipliers l_V and l_C, the penalizers c_V and c_C, the effective objective function is then

$$\mathcal{L}_\Omega(\Omega,\Gamma,l_V,l_C;c_V,c_C) = \mathcal{L}_{\Omega,A}(\Omega,\Gamma,l_C;c_V,c_C) + l_V\,\mathcal{L}_{\Omega,B}(\Omega,\Gamma,l_C;c_V,c_C), \tag{35}$$

with

$$\begin{cases} \mathcal{L}_{\Omega,A}(\Omega,\Gamma,l_C;c_V,c_C) = \dfrac{C_{\text{ply}}(\Omega)}{\overline{C_{\text{ply}}}^0} + \dfrac{L_\Gamma(\Gamma)}{\overline{L_\Gamma}^0} + \dfrac{c_V}{2}\left(\dfrac{V(\Omega)-V^{\text{target}}}{\overline{V}^0}\right)^2 + l_C\dfrac{C(\Omega,\Gamma)}{\overline{C}^0} + \dfrac{c_C}{2}\left(\dfrac{C(\Omega,\Gamma)}{\overline{C}^0}\right)^2, \\ \mathcal{L}_{\Omega,B}(\Omega) = \dfrac{V(\Omega)-V^{\text{target}}}{\overline{V}^0} \end{cases} \tag{36}$$

where $\overline{C_{\text{ply}}}^0 = C_{\text{ply}}(\Omega^0)$, $\overline{L_\Gamma}^0 = L_\Gamma(\Gamma^0)$, $\overline{V}^0 = V(\Omega^0)$ and $\overline{C}^0 = C(\Omega^0,\Gamma^0)$. The gradient to this effective objective function is then computed as $\mathcal{L}'^\Omega_\Omega = \mathcal{L}'^\Omega_{\Omega,A} + l_V\,\mathcal{L}'^\Omega_{\Omega,B}$, with

$$\begin{cases} \mathcal{L}'^\Omega_{\Omega,A}(\Omega,\Gamma,l_C;c_V,c_C) = \dfrac{C'^\Omega_{\text{ply}}(\Omega)}{\overline{C_{\text{ply}}}^0} + \dfrac{c_V}{\left(\overline{V}^0\right)^2}V'^\Omega(\Omega) + \left(\dfrac{l_C}{\overline{C}^0} + \dfrac{c_C}{\left(\overline{C}^0\right)^2}C(\Omega,\Gamma)\right)C'^\Omega(\Omega,\Gamma), \\ \mathcal{L}'^\Omega_{\Omega,B}(\Omega) = \dfrac{V'^\Omega(\Omega)}{\overline{V}^0} \end{cases} \tag{37}$$

The descent direction $d_\Omega^{n_\Omega}$ involved in the Hamilton Jacobi equation (34) is related to this gradient and the following advection step (see Algorithm 2):

$$s_\Omega^k = \text{Coef}_\Omega^k \frac{\Delta x}{\|d_\Omega^{n_\Omega}\|_{L^\infty}}, \tag{38}$$

with Coef_Ω^k initialized to 5 and updated so that

$$\begin{cases} \min(1.2\,\text{Coef}_\Omega^k, 1), & \mathcal{L}_\Omega(\Omega^{k+1},\Gamma^{k+1},l_V^k,l_C^k;c_V,c_C) \leq \text{tol}_\Omega^k * \mathcal{L}_\Omega(\Omega^k,\Gamma^k,l_V^k,l_C^k;c_V,c_C), \\ 0.6\,\text{Coef}_\Omega^k, & \text{else.} \end{cases} \tag{39}$$

The tolerance tol_Ω initialized to 1.6 and multiplied by 0.9 every 50 iterations. The final algorithm is given by Algorithm 2 with further details in [26] Chapter 9.
The coefficient $\varepsilon_{\text{dicho}}$ is initialized to 0.05 and multiplied by 0.95 at each iteration during the 120 first ones. The volume tolerance is then fixed to $\varepsilon_{\text{dicho}} = 1.1\,10^{-4}$.

initialize the shape and path Ω^0, Γ^{-1}, $c_V = 1$, $l_C^0 = 1$, $c_C = 1$,
compute the optimal path Γ^0 (application of Algorithm 1 initialized by Γ^{-1} with N_Γ^0),
initialize of l_V,
for $it_\Omega \in [\![0, N_\Omega]\!]$ **do**
    determine by a dichotomy l_V^{test} such that $|V(\Omega^{\text{test}}) - V^{\text{target}}| \leq \varepsilon_{\text{dicho}}$,
    compute the new compliance $C_{\text{ply}}(\Omega)$ and volume $V(\Omega)$,
    determination of the optimal Γ (application of Algorithm 1 initialized by Γ^{it_Ω} with $N_\Gamma^{it_\Omega}$), $L_\Gamma(\Gamma)$, $C(\Omega, \Gamma)$),
    if $\mathcal{L}_\Omega(\Omega, \Gamma, l_V^{it_\Omega}, l_C^{it_\Omega}; c_V, c_C) \leq tol_\Omega \mathcal{L}_\Omega(\Omega^{it_\Omega}, \Gamma^{it_\Omega}, l_V^{it_\Omega}, l_C^{it_\Omega}; c_V, c_C)$ **then**
        iteration accepted: $\Omega^{it_\Omega+1} = \Omega$, $\Gamma^{it_\Omega+1} = \Gamma$,
        update the Lagrange multiplier $l_V^{it_\Omega+1} = l_V^{\text{test}} + c_V V^{it_\Omega+1}$,
        update the Lagrange multiplier $l_C^{it_\Omega} + c_C C^{it_\Omega+1}$,
        compute the new objective function and gradients,
        increase the step coefficient related to the shape: $\text{Coef}_\Omega = \min(1.2\,\text{Coef}_\Omega, 5)$
    end
    else
        iteration rejected (shape and path rejected),
        decrease the step coefficient related to the shape: $\text{Coef}_\Omega = 0.6\,\text{Coef}_\Omega$.
    end
end

Algorithm 2: Iterative double loop algorithm to optimize the shape and the path.

Remark 6. *In this outer loop, the augmented Lagrangian algorithm is supplemented by a dichotomy on the volume Lagrange multiplier. Indeed, as stated in Remark 4, the augmented Lagrangian ensures the fulfilment of the constraints at convergence only. However, we cannot make sure here that the volume constraint is satisfied which explains why adding this second method. Note that if this method can be very easily adapted to the volume, it could not be implemented at such a cheap cost for the temperature contraint. Indeed, modifying the volume does not involve any partial differential equation whereas the temperature constraint not only involves a heat equation but also the resolution of an inner loop, drastically increasing the computational costs of a dichotomy on its coefficients.*

5 Numerical results

An initialization state INI is defined with a shape Ω^{INI} and a path Γ^{INI} (subfigure (a) in each Figure). From Algorithm 2, different tests are run, summed up in Figure 6:

- SONLY: **shape optimized - path fixed**, without any consideration of the temperature constraints ($l_C = 0$ and $c_C = 0$). This test is initialized with $\Omega^0 = \Omega^{\text{INI}}$.
- STEMP: **shape optimized - path fixed**, taking into consideration the temperature constraints ($l_C^0 = 1$, $c_C = 1$, $\forall it_\Omega \in [\![0, N_\Omega]\!]$, $N_\Gamma^{it_\Omega} = 0$). This test is initialized with $\Omega^0 = \Omega^{\text{INI}}$ and the fixed path used for the temperature computations is Γ^{INI}.
- SP-fromINI: **shape optimized - path optimized**. This test optimizes both variables taking into account temperature constraints ($l_C^0 = 1$, $c_C = 1$). The number of inner loop iterations follows Table 1. Recall that the inner loop is also broken when the inner loop step coefficient is smaller than 10^{-8}. This test is initialized with $\Omega^0 = \Omega^{\text{INI}}$ and $\Gamma^0 = \Gamma^{\text{INI}}$.

it_Ω	$[\![0,24]\!]$	25	$[\![26,44]\!]$	45	$[\![46,49]\!]$	50	$[\![51,54]\!]$	55	56	57	58	59	$[\![60,300]\!]$
$N_\Gamma^{it_\Omega}$	0	50	0	45	0	40	0	35	30	25	20	15	10

Table 1: Number of inner loop maximum number of iterations N_Γ depending on the outer loop iteration it_Ω.

- PONLY: **shape fixed - path optimized**. This test is initialized by $\Gamma^0 = \Gamma^{\text{INI}}$ and the fixed shape to build is Ω^{SONLY} resulting from the optimization test SONLY. This test only involves the inner loop and in this case only, the tolerance of the inner loop is initialized to 2 and multiplied by 0.9 every 50 iterations.
- SP-fromPONLY: **shape optimized - path optimized**. This test optimizes both variables taking into account temperature constraints ($l_C^0 = 1$, $c_C = 1$). The number of inner loop iterations follows Table 1.

Recall that if the inner loop is also broken when the inner loop step coefficient is smaller than 10^{-8}. This test is initialized with the shape $\Omega^0 = \Omega^{\text{SONLY}}$ resulting from the optimization test SONLY and with the path $\Gamma^0 = \Gamma^{\text{PONLY}}$ resulting from the optimization test PONLY.

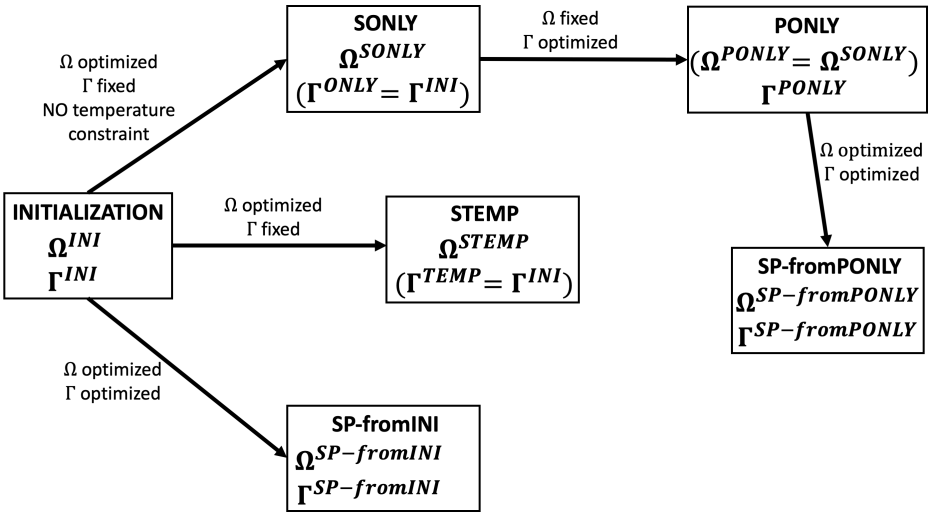

Figure 6: Recap scheme of the different tests

For all these tests, the regularization coefficients are $\nu_\Omega = 5\Delta x$ and $\nu_\Gamma = 15 d_{\text{lower}}$. For each of these tests, the final shape, path and temperature are given. A table sums up the final compliance, volume, path length and adimensionalized temperature constraints defined by:

$$\overline{C_\phi} = \frac{C_\phi}{|\Omega| y_\phi^2}, \quad \overline{C_{M,\Omega}} = \frac{C_{M,\Omega}}{|\Omega| y_{M,\Omega}^2}, \quad \overline{C_{M,D\setminus\Omega}} = \frac{C_{M,D\setminus\Omega}}{|D\setminus\overline{\Omega}| y_{M,D\setminus\Omega}^2}. \tag{40}$$

A final radar chart sums up the quantitative results. Note that in these graphs, for each of the functions represented (compliance and temperature constraints), the axes are reversed so that the best solutions correspond to the curve with the biggest area.

5.1 Cantilever test case

The first test case is a cantilever. A symmetry condition is applied and the working domain is $D = [-1.4, 1.4] \times [0, 0.7]$ given in *mm* (full domain corresponding to $[-1.4, 1.4] \times [-0.7, 0.7]$. This working domain is meshed with 12800 triangular elements. As only half of the working domain is considered for symmetry reasons, the point of the path initially belonging to the (Ox)-axis is constrained to remain on this axis. This constraint comes from the will, in this work, to focus on a path composed of only one connected component. Allowing this feature to be modified would impact the numerical results and is part of the perspectives.

Two different physical cases are consider in the following: the aluminium and the titanium. In both cases, the Poisson ratio is set to $\nu = 0.3$, the Young coefficient to $E = 1 k_g m^{-1} s^{-2}$ and the loading to $h = (0, -2)$ in $k_g m s^{-2}$. These values do not correspond to real values but, because there exists a linear relation between the displacement and the Young coefficient, they could easily be modified. As for the parameters involved in the heat equation, they are summed up in Table 2. The power P and the coefficient β are determined using a calibration process detailed in [26] Chapter 4. In both cases, the initial temperature is fixed to $y_{\text{ini}} = 773K$.

Metal	$\lambda\,(Wm^{-1}K^{-1})$	$P\,(Ws^{-1}m^{-1})$	$\beta\,(WK^{-1}m^{-3})$	$y_\phi\,(K)$	$y_{M,\Omega}\,(K)$	$y_{M,D\setminus\Omega}\,(K)$
Aluminium	130	$400 * 5.45 * 10^6$	$\frac{\lambda}{2.21 * 10^{-9}}$	870	1670	870
Titanium	15	$300 * 5.45 * 10^6$	$\frac{\lambda}{2.21 * 10^{-9}}$	1900	3400	1800

Table 2: Numerical values chosen in the aluminium and titanium test cases.

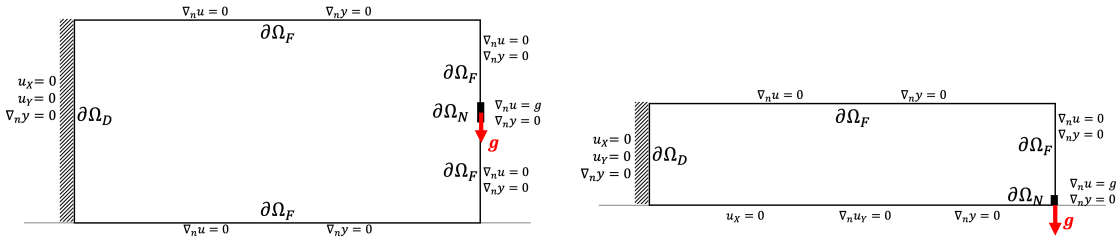

(a) Non symmetric test case

(b) Symmetric test case

Figure 7: Cantilever test case with the symmetry conditions for the mechanical and heat problems

For each of the aluminium and titanium test cases, two different volume ratios are tested: $V^{\text{target}} = 0.9V^0$ and $V^{\text{target}} = 1.1V^0$ with $V^0 = 1.157e-06m^2$.

In most of the following Figures, only half of the cantilever is shown. Indeed, for symmetry reasons, the optimization is run on half the working domain only. To get the full result, the Figures should be symmetrized with respect to the horizontal lower axis.

5.1.1 Aluminium test case

For the aluminium, the results of the five tests for each volume ratio are respectively presented in Figures 8 and 9 as well as Table 3 for $V^{\text{target}} = 0.9V^0$ and Figures 10 and 11 as well as Table 4 for $V^{\text{target}} = 1.1V^0$.

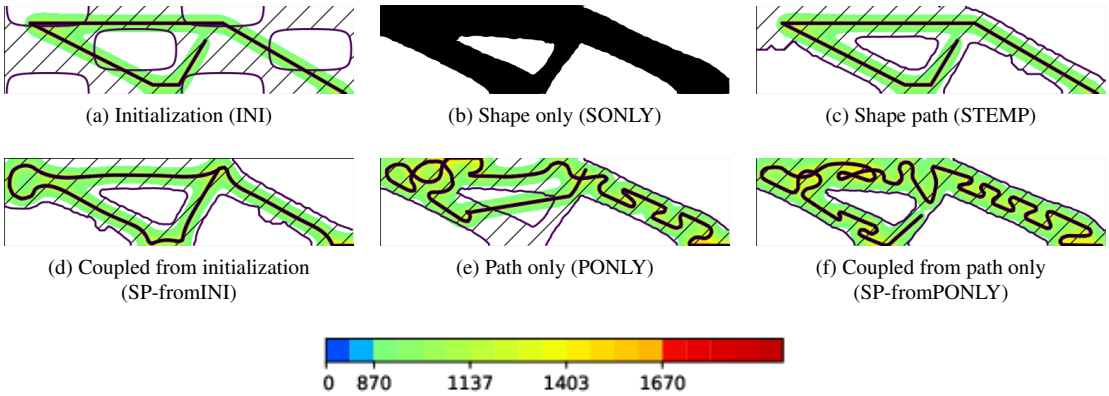

(a) Initialization (INI)

(b) Shape only (SONLY)

(c) Shape path (STEMP)

(d) Coupled from initialization (SP-fromINI)

(e) Path only (PONLY)

(f) Coupled from path only (SP-fromPONLY)

(g) Temperature colorbar (K)

Figure 8: Initialization and shape optimization for different tests, aluminium, half cantilever, $V^{\text{target}} = 0.9V^0$

case	$\frac{V}{V^0}$	$C_{\text{ply}}\,(k_g m s^{-2})$	$L_\Gamma\,(m)$	$\overline{C_\phi}$	$\overline{C_{M,\Omega}}$	$\overline{C_{M,D\setminus\Omega}}$
INI	1.00	$5.67e-06$	$4.38e-03$	$4.88e-03$	$0.00e+00$	$7.30e-03$
SONLY	0.90	$2.25e-06$	$4.38e-03$	$1.70e-03$	$0.00e+00$	$1.47e-03$
STEMP	0.90	$2.35e-06$	$4.38e-03$	$1.27e-03$	$0.00e+00$	$1.22e-07$
SP-fromINI	0.90	$2.38e-06$	$5.40e-03$	$4.93e-04$	$0.00e+00$	$3.70e-07$
PONLY	0.90	$2.25e-06$	$7.35e-03$	$1.29e-03$	$9.91e-10$	$2.82e-03$
SP-fromPONLY	0.90	$2.26e-06$	$8.32e-03$	$1.90e-05$	$0.00e+00$	$2.72e-05$

Table 3: Quantitative results for the different tests, aluminium, half cantilever, $V^{\text{target}} = 0.9V^0$

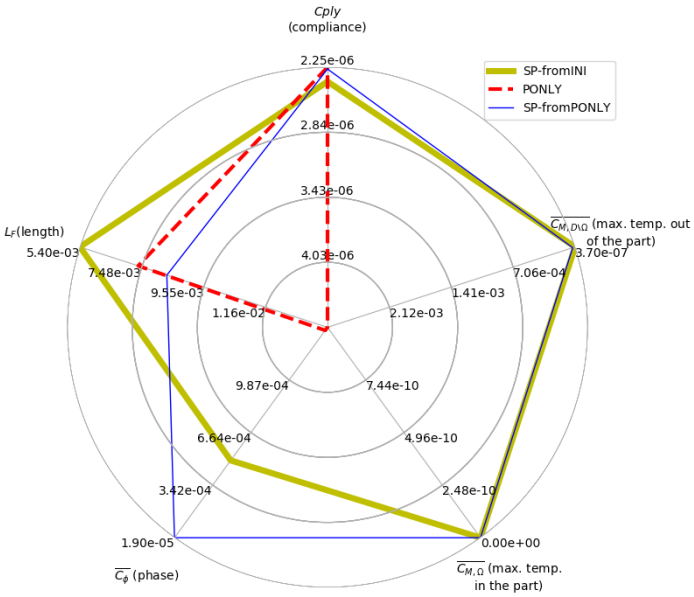

Figure 9: Radar chart of the values given in Table 3 (but for the volume), aluminium, half cantilever, $V^{\text{target}} = 0.9V^0$

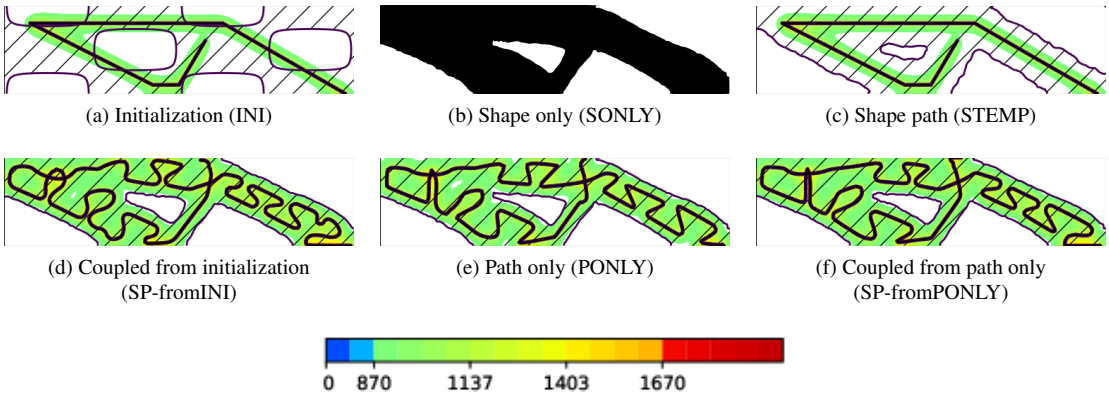

(a) Initialization (INI)

(b) Shape only (SONLY)

(c) Shape path (STEMP)

(d) Coupled from initialization (SP-fromINI)

(e) Path only (PONLY)

(f) Coupled from path only (SP-fromPONLY)

(g) Temperature colorbar (K)

Figure 10: Initialization and shape optimization for different tests, aluminium, half cantilever, $V^{\text{target}} = 1.1V^0$

case	$\frac{V}{V^0}$	$C_{\text{ply}}\,(k_g m s^{-2})$	$L_\Gamma\,(m)$	$\overline{C_\phi}$	$\overline{C_{M,\Omega}}$	$\overline{C_{M,D\setminus\Omega}}$
INI	1.00	$5.67e-06$	$4.38e-03$	$4.88e-03$	$0.00e+00$	$7.30e-03$
SONLY	1.10	$1.92e-06$	$4.38e-03$	$2.47e-03$	$0.00e+00$	$1.40e-05$
STEMP	1.10	$2.00e-06$	$4.38e-03$	$2.22e-03$	$0.00e+00$	$0.00e+00$
SP-fromINI	1.10	$1.92e-06$	$9.57e-03$	$9.98e-06$	$0.00e+00$	$1.39e-05$
PONLY	1.10	$1.92e-06$	$8.85e-03$	$1.66e-05$	$0.00e+00$	$1.99e-05$
SP-fromPONLY	1.10	$1.92e-06$	$9.34e-03$	$1.10e-05$	$0.00e+00$	$1.48e-05$

Table 4: Quantitative results for the different tests, aluminium, half cantilever, $V^{\text{target}} = 1.1V^0$

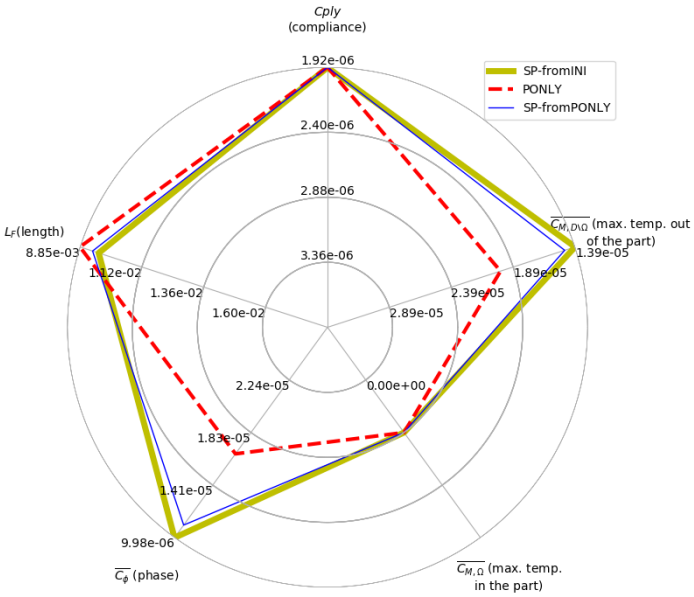

Figure 11: Radar chart of the values given in Table 4 (but for the volume), aluminium, half cantilever, $V^{\text{target}} = 1.1V^0$

The results coming from both volume constraints ($V = 0.9V^0$ and $V = 1.1V^0$) lead to the same kind of observations. First of all, it is clear that introducing temperature constraints impacts the part's shape. Indeed, in both Figures 8 and 10, the shape presented in (b) is different than in (c) whereas in both tests the path is maintained unmodified and the only difference is the inclusion of temperature constraints in (c). In (c), the lower right bar is thickened to reduce the maximum temperature constraint out of the shape whereas the other bars (upper right in Figure 8 and lower left in 10) are made thinner. Figures (c) also make really clear how fixing the volume impacts the optimization: the shape cannot exactly adapt to the path and reduce the phase constraint since this would require decreasing the volume which is prevented by the dichotomy (see Table 3 and 4).
The optimization of the path only (shape fixed to the result from SONLY, Figures (b)) presented by Figures 8 (e) and 10 (e) is also very informative. In Figure 8 (e), this optimization fails: the phase constraint is not satisfied and the path crosses a zone out of the shape to build. Indeed, it seems complicated for the path to build the right lower bar: the conductivity is high and the path cannot cross this bar without violating the maximum temperature constraint out of the domain. Struggling to remedy to this problem, the optimization ends up by being stuck into a local minimum that does not satisfy the temperature constraints. On the contrary in Figure 10 (e), the bar is thicker and the path optimization satisfies well the constraints. Note that besides the correct respect of the constraints, the path shown on Figure 10 (e) presents a cross-over. Preventing these auto-intersections could come from a better formulation of the maximum temperature constraint within the part Ω but remain part of the perspectives. Note also that both path optimizations could give different results if more than one path connected component were allowed. If some methods allowing this feature in path optimization have been developed (see [26] Chapter 8), including them in concurrent path and part optimization remains part of the perspectives.
Finally, coupled optimizations are run in each case starting from two different initializations: from Figure (a) to Figure (d) and from Figure (e) to Figure (f). In Figure 8, the strategies are different from one initialization to another. Starting from (a) to (d), the result looks like a simple adaptation of (c): the path is slightly adapted to increase the volume built thus fitting the volume constraint required on the shape whereas the shape's boundary really adapts to the melted zones (upper left corner for example). Starting from (e), the bars thickness are not modified much. The modifications simply allow the path to get out of the local minimum and ends the optimization process. In Figure 10, both initializations lead to similar results. One can especially notice the Omega-patterns chosen by the path to correctly build the different bars. This pattern was already used in Figure 8 (f).

From these first results, two main points are pointed out. First, the importance of the initialization: corroborating the results detail in [26, 25], it seems that the several local minima related to path optimization impact the concurrent optimization results. This initialization should then be chosen with care depending on the optimization context.
Then, if the results cannot lead to design optimization constraints yet, it is very clear that the bars thickness are crucial. Indeed, in each concurrent optimization test, the thin bars have been thickened until they almost

correspond to the thickness of the melted powder domain generated by the source. Moreover, not only does the bars thickness determine the ability for path optimization to satisfy the constraints but it also impacts the pattern used by this very optimal path: a too thin bar (with respect to conductivity and power) cannot be built, a thin bar is dealt with by a straight line path, a thicker bar involves Omega-shape patterns. A first design optimization criterion could thus be the thickness of the bars to build and an interesting perspective would be to compare the results obtained for design under thickness constraints (see [52]) to the concurrent design of shape and scanning path.

The optimization on the whole working domain is finally run to evaluate the impact of the symmetry. For $V^{\text{target}} = 0.9V^0$, the results are shown in Figure 12 and Table 5.

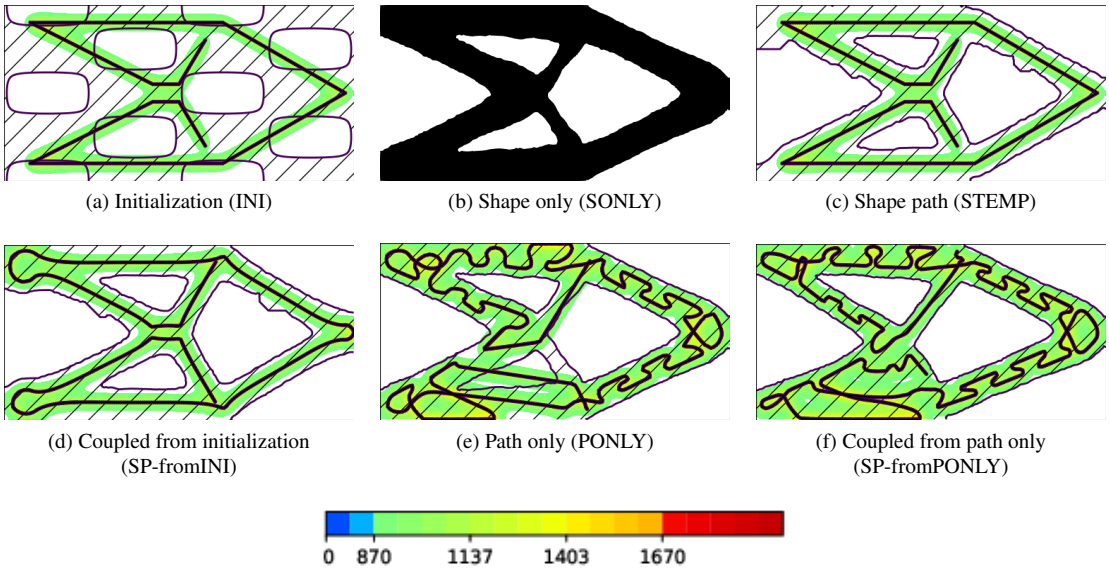

(a) Initialization (INI)
(b) Shape only (SONLY)
(c) Shape path (STEMP)
(d) Coupled from initialization (SP-fromINI)
(e) Path only (PONLY)
(f) Coupled from path only (SP-fromPONLY)
(g) Temperature colorbar (K)

Figure 12: Initialization and shape optimization for different tests, aluminium, full cantilever, $V^{\text{target}} = 0.9V^0$

case	$\frac{V}{V^0}$	C_{ply}	L_Γ	$\overline{C_\phi}$	$\overline{C_{M,\Omega}}$	$\overline{C_{M,D\setminus\Omega}}$
INI	1.00	$1.13e-05$	$8.77e-03$	$4.88e-03$	$0.00e+00$	$7.30e-03$
SONLY	0.90	$4.49e-06$	$8.77e-03$	$1.63e-03$	$0.00e+00$	$1.11e-03$
STEMP	0.90	$4.72e-06$	$8.77e-03$	$1.16e-03$	$0.00e+00$	$4.45e-08$
SP-fromINI	0.90	$4.67e-06$	$1.02e-02$	$5.22e-04$	$0.00e+00$	$3.77e-08$
PONLY	0.90	$4.49e-06$	$1.59e-02$	$1.44e-04$	$0.00e+00$	$1.85e-03$
SP-fromPONLY	0.90	$4.56e-06$	$1.60e-02$	$1.77e-05$	$0.00e+00$	$3.05e-05$

Table 5: Quantitative results for the different tests, aluminium, full cantilever, $V^{\text{target}} = 0.9V^0$

If the results from Figure 12 (a-b-c-d) are very similar to Figure 8 (a-b-c-d), it seems in the optimization of the path only (e) that the path symmetry has been broken. In Figure 8 (e), the path has already difficulties to cross the right lower bar. In Figure 12 (e), it manages to cross it yet encroaching on the lower half of the Figure thus preventing the same method for the symmetric to this right lower bar. Note also that on the right and middle of the Figure (junction location in Figure 8 (e)), the path is not horizontal anymore but introduces an intersection. As for Figure 12 (f), it cannot be symmetric because starting from a non symmetric initialization, and induces the loss of the lower hole. Yet, the shape evolution allows for a correct satisfaction of the constraints.

5.1.2 Titanium test case

For the titanium, the results of the five tests for each volume ratio are presented by Figure 13 and 14 as well as Table 6 for $V^{\text{target}} = 0.9V^0$ and Figure 15 and 16 as well as Table 7 for $V^{\text{target}} = 1.1V^0$.

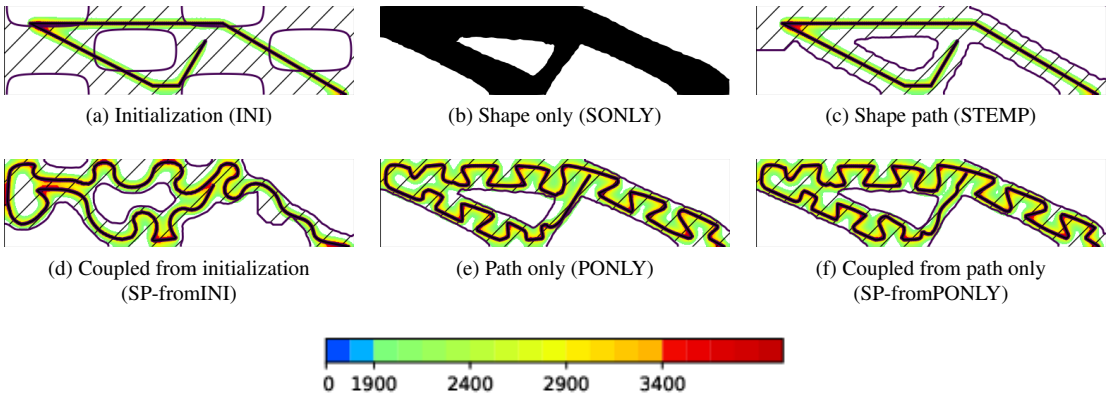

(a) Initialization (INI) (b) Shape only (SONLY) (c) Shape path (STEMP)

(d) Coupled from initialization (SP-fromINI) (e) Path only (PONLY) (f) Coupled from path only (SP-fromPONLY)

(g) Temperature colorbar (K)

Figure 13: Initialization and shape optimization for different tests, titanium, half cantilever, $V^{\text{target}} = 0.9V^0$

case	$\frac{V}{V^0}$	$C_{\text{ply}}\,(k_g m s^{-2})$	$L_\Gamma\,(m)$	$\overline{C_\phi}$	$\overline{C_{M,\Omega}}$	$\overline{C_{M,D\setminus\Omega}}$
INI	1.00	$5.67e-06$	$4.38e-03$	$1.69e-01$	$2.79e-05$	$2.29e-02$
SONLY	0.90	$2.25e-06$	$4.38e-03$	$8.91e-02$	$1.55e-04$	$3.93e-03$
STEMP	0.90	$2.36e-06$	$4.38e-03$	$7.56e-02$	$1.55e-04$	$0.00e+00$
SP-fromINI	0.90	$3.37e-06$	$7.40e-03$	$1.91e-02$	$3.78e-04$	$1.34e-04$
PONLY	0.90	$2.25e-06$	$8.63e-03$	$2.14e-03$	$1.10e-04$	$2.25e-04$
SP-fromPONLY	0.90	$2.25e-06$	$8.63e-03$	$1.66e-03$	$1.24e-04$	$1.45e-04$

Table 6: Quantitative results for the different tests, titanium, half cantilever, $V^{\text{target}} = 0.9V^0$

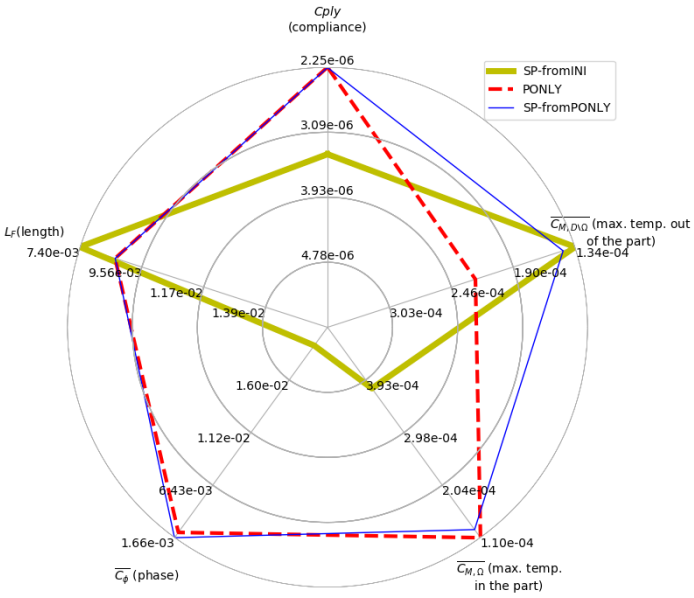

Figure 14: Radar chart of the values given in Table 6 (but for the volume), titanium, half cantilever, $V^{\text{target}} = 0.9V^0$

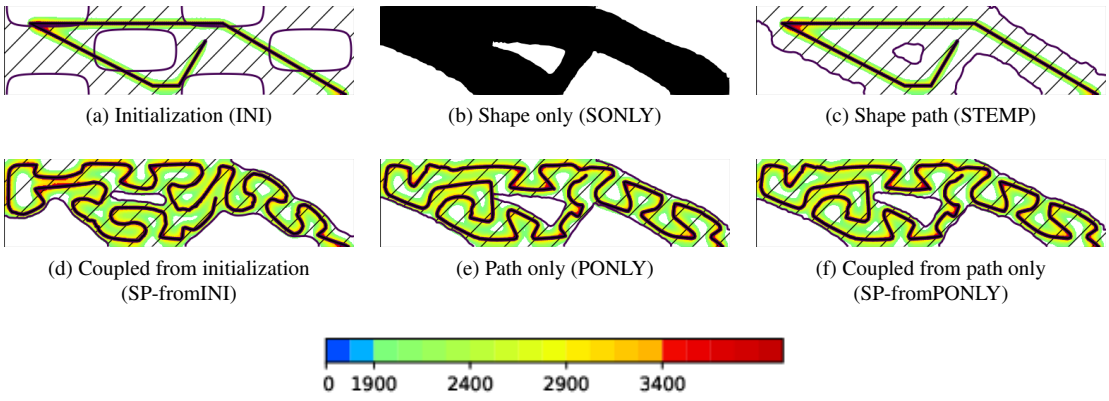

(a) Initialization (INI) (b) Shape only (SONLY) (c) Shape path (STEMP)

(d) Coupled from initialization (SP-fromINI) (e) Path only (PONLY) (f) Coupled from path only (SP-fromPONLY)

(g) Temperature colorbar (K)

Figure 15: Initialization and shape optimization for different tests, titanium, half cantilever, $V^{\text{target}} = 1.1V^0$

case	$\frac{V}{V^0}$	$C_{\text{ply}}\,(k_g m s^{-2})$	$L_\Gamma\,(m)$	$\overline{C_\phi}$	$\overline{C_{M,\Omega}}$	$\overline{C_{M,D\setminus\Omega}}$
INI	1.00	$5.67e-06$	$4.38e-03$	$1.69e-01$	$2.79e-05$	$2.29e-02$
SONLY	1.10	$1.92e-06$	$4.38e-03$	$1.13e-01$	$1.26e-04$	$0.00e+00$
STEMP	1.10	$2.12e-06$	$4.38e-03$	$1.08e-01$	$1.26e-04$	$0.00e+00$
SP-fromINI	1.10	$2.14e-06$	$1.02e-02$	$3.05e-03$	$1.41e-04$	$6.08e-05$
PONLY	1.10	$1.92e-06$	$1.00e-02$	$1.39e-03$	$9.73e-05$	$3.67e-04$
SP-fromPONLY	1.10	$1.92e-06$	$1.00e-02$	$1.20e-03$	$9.74e-05$	$5.01e-05$

Table 7: Quantitative results for the different tests, titanium, half cantilever, $V^{\text{target}} = 1.1V^0$

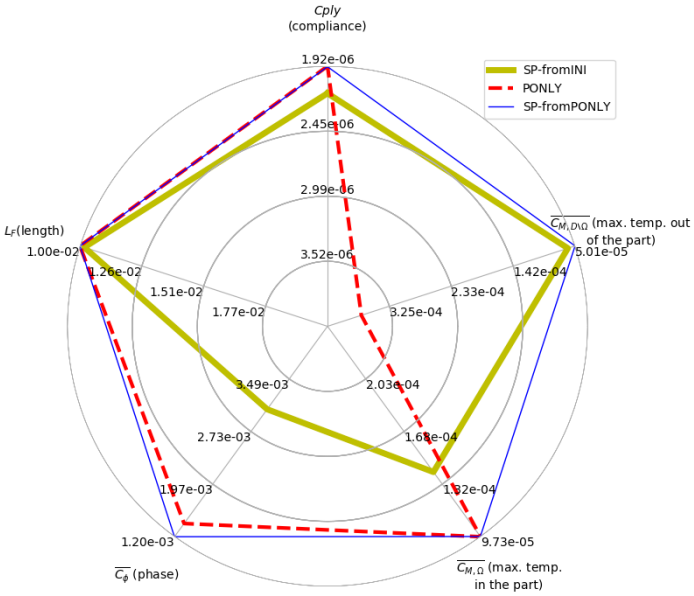

Figure 16: Radar chart of the values given in Table 7 (but for the volume), titanium, half cantilever, $V^{\text{target}} = 1.1V^0$

First of all, the results obtained corroborate the observations coming from the aluminium test case.
The initialization matters, even more in the titanium case because of this metal's low conductivity. In both Figures 13 and 15, the results from concurrent optimization given in (d) (initialized by (a)) and given in (f) (initialized by (e)) are different: because the titanium conductivity is small, the shape is highly modified in concurrent optimization starting from (c): the phase constraint is far from being fulfilled at initialization. On the contrary, the shape slightly adapts when starting from PONLY (e) since the phase constraint is well satisfied. The path and shape are only adapted to fit the zones that remain unmelted.
Then, the bars thickness is important. The conductivity of the titanium is lower than the aluminium's. If this makes easier for the path to cross thin lines, it complicates the filling of thick ones. This leads to more complex

structures with oscillations of the part's boundary to fit the melted zones (Figure 13). This also impacts the patterns used to design the path, with once again straight line and Omega-shape patterns.

Remark 7. *it is recalled that the Young modulus for the aluminium and for the titanium have been both chosen equal to* $E = 1 k_g m^{-1} s^{-2}$. *This does not correspond to the real Young modulus for each metal but does not change the theory nor the type of results obtained yet facilitating the numerical tests. For the titanium though, the bars could be thinner than obtained in this article.*

The optimization on the whole working domain is finally run to evaluate the impact of the symmetry. For $V^{\text{target}} = 0.9V^0$, the results are shown in Figure 17 and Table 8.

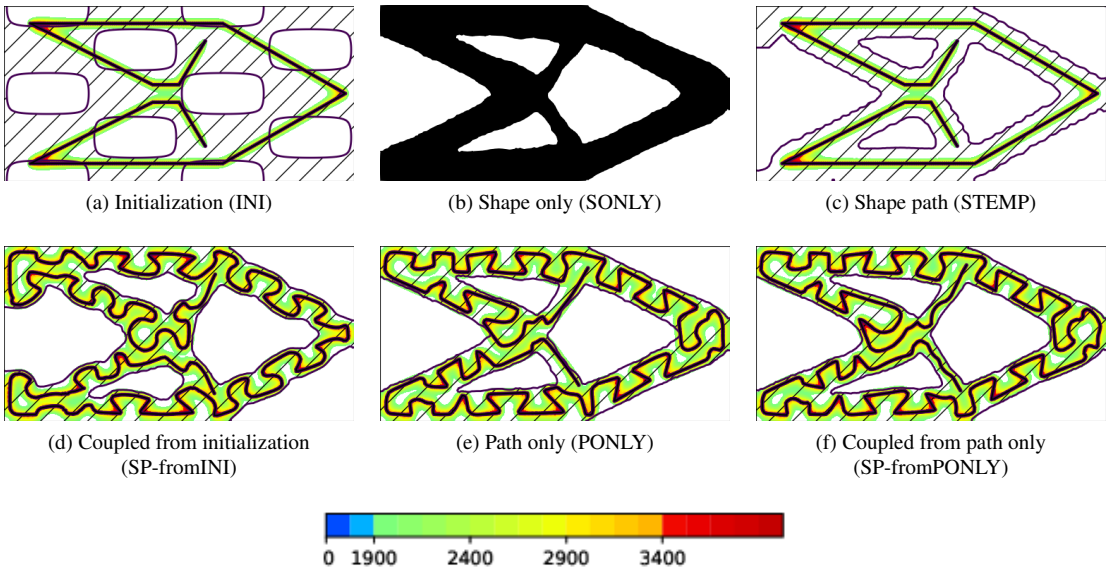

(a) Initialization (INI) (b) Shape only (SONLY) (c) Shape path (STEMP)

(d) Coupled from initialization (SP-fromINI) (e) Path only (PONLY) (f) Coupled from path only (SP-fromPONLY)

(g) Temperature colorbar (K)

Figure 17: Initialization and shape optimization for different tests, titanium, full cantilever, $V^{\text{target}} = 0.9V^0$

case	$\frac{V}{V^0}$	$C_{\text{ply}}\,(k_g m s^{-2})$	$L_\Gamma\,(m)$	$\overline{C_\phi}$	$\overline{C_{M,\Omega}}$	$\overline{C_{M,D\setminus\Omega}}$
INI	1.00	$1.13e-05$	$8.77e-03$	$1.69e-01$	$2.79e-05$	$2.29e-02$
SONLY	0.90	$4.49e-06$	$8.77e-03$	$8.70e-02$	$1.55e-04$	$2.77e-03$
STEMP	0.90	$4.96e-06$	$8.77e-03$	$7.29e-02$	$1.55e-04$	$0.00e+00$
SP-fromINI	0.90	$4.92e-06$	$1.76e-02$	$1.92e-03$	$1.46e-04$	$6.76e-05$
PONLY	0.90	$4.49e-06$	$1.73e-02$	$2.68e-03$	$1.12e-04$	$8.20e-04$
SP-fromPONLY	0.90	$4.50e-06$	$1.74e-02$	$2.02e-03$	$1.61e-04$	$1.45e-04$

Table 8: Quantitative results for the different tests, titanium, full cantilever, $V^{\text{target}} = 0.9V^0$

As for the aluminium, dealing with the entire geometry induces slight unsymmetries especially to correctly melt the middle zone. Yet, the results remain quite similar with the use of the Omega-pattern and the boundary adaptations to the temperature constraints.

5.2 Large cantilever test case

The first test case points out that shape and path are related through the thickness of the bars composing the shape (combined to the conductivity and source power). In this second test case, the working domain size is increased: the final shape is supposed to be bigger and thus thicker than previously. The objective is to confirm, in these new conditions, the results already obtained.

The second test case features the same cantilever but in a larger working domain which, with the symmetry condition, amounts to $D = [-2.8, 2.8] \times [0, 1.4]$ given in *mm*. Because the physical parameters are kept unchanged in the heat equation, the problem is not scale-invariant. To keep the same accuracy in the source description and the temperature computation, the mesh of this new working domain should be as thin as the previous mesh and thus be composed of 51200 triangular elements. However, with such a number of elements, the computational costs coming from the resolution of the mechanical problem at each outer loop

iteration would be far too high. In the inner loop however, the rigidity matrix related to the heat equation remains the same during the whole optimization process and must be inverted only once. Two different meshes are used: the outer loop and the mechanical computations are run using a mesh with 12800 elements, the inner loop is run with the thin mesh. Then, to allow for the computation of the shape derivatives, the temperature computed on the thin mesh is interpolated (classic interpolation in FreeFem++ [53]) on the outer loop mesh. The mechanical settings remain the same (see Figure 7): for both the titanium and aluminium, the Poisson ratio is fixed to $\nu_e = 0.3$, the Young coefficient is $E_e = 1$ and the loading $h = (0, -2)$ and the heat equation coefficients follow Table 2. For both the aluminium and the titanium test cases, two path initializations are tested. In both cases, the initial volume is $V^0 = 4.629e-06m^2$.

5.2.1 Aluminium test case

The results for the volume constraint $V^{\text{target}} = 0.9V^0$ are given by Figure 18, Table 9 and Figure 19 for the first initialization and Figure 20, Table 10 and Figure 21 for the second.

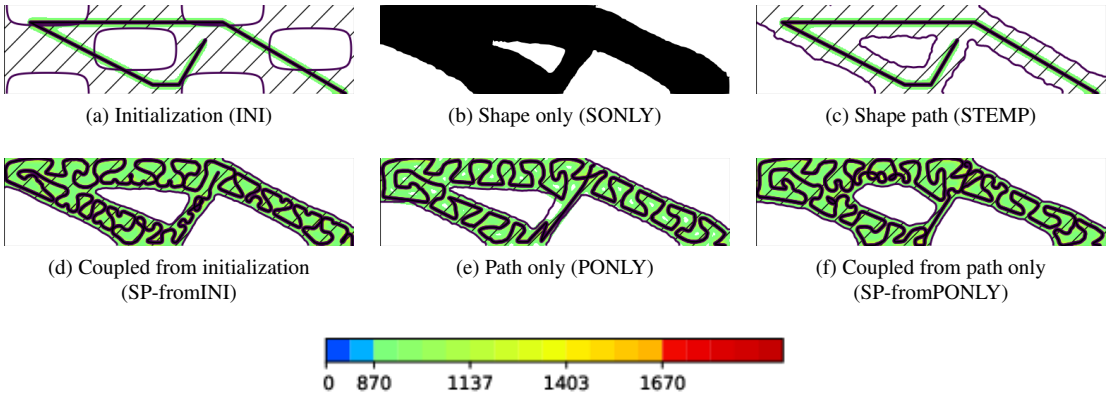

(a) Initialization (INI)
(b) Shape only (SONLY)
(c) Shape path (STEMP)
(d) Coupled from initialization (SP-fromINI)
(e) Path only (PONLY)
(f) Coupled from path only (SP-fromPONLY)
(g) Temperature colorbar (K)

Figure 18: Initialization and shape optimization for different tests, initialization 1, aluminium, half large cantilever, $V^{\text{target}} = 0.9V^0$

case	$\frac{V}{V^0}$	$C_{\text{ply}}\,(k_g m s^{-2})$	$L_\Gamma\,(m)$	$\overline{C_\phi}$	$\overline{C_{M,\Omega}}$	$\overline{C_{M,D\setminus\Omega}}$
INI	1.00	$2.27e-05$	$8.77e-03$	$8.07e-03$	$0.00e+00$	$3.54e-03$
SONLY	0.90	$9.052e-06$	$8.765e-03$	$6.014e-03$	$0.000e+00$	$9.194e-04$
STEMP	0.90	$9.44e-06$	$8.77e-03$	$5.45e-03$	$0.00e+00$	$0.00e+00$
SP-fromINI	0.90	$9.01e-06$	$2.99e-02$	$7.07e-06$	$0.00e+00$	$1.20e-05$
PONLY	0.90	$9.05e-06$	$2.63e-02$	$6.02e-05$	$0.00e+00$	$1.28e-04$
SP-fromPONLY	0.90	$9.37e-06$	$2.98e-02$	$5.56e-06$	$0.00e+00$	$7.55e-06$

Table 9: Quantitative results for the different tests, initialization 1, aluminium, half large cantilever, $V^{\text{target}} = 0.9V^0$

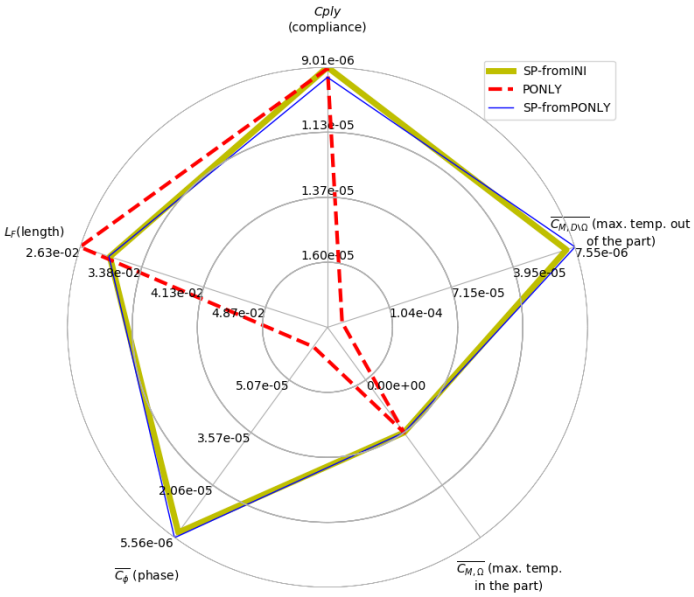

Figure 19: Radar chart of the values given in Table 9 (but for the volume), initialization 1, aluminium, half large cantilever, $V^{\text{target}} = 0.9V^0$

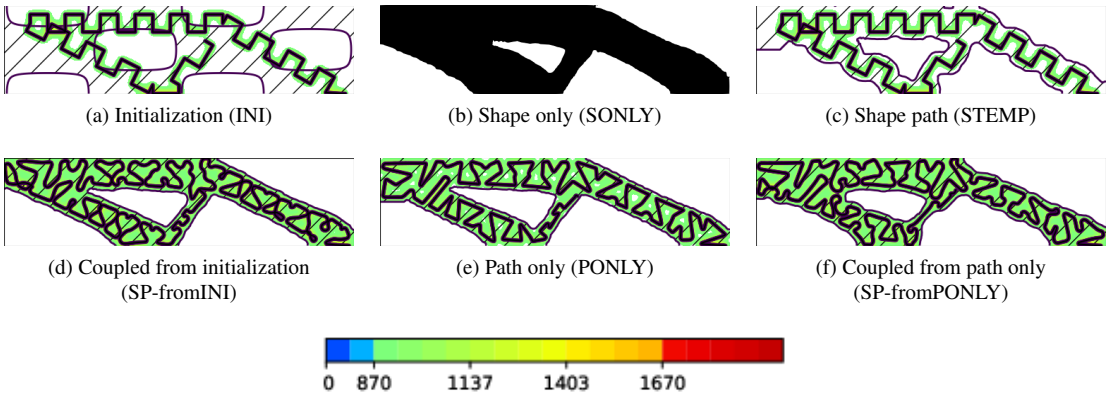

(a) Initialization (INI)

(b) Shape only (SONLY)

(c) Shape path (STEMP)

(d) Coupled from initialization (SP-fromINI)

(e) Path only (PONLY)

(f) Coupled from path only (SP-fromPONLY)

(g) Temperature colorbar (K)

Figure 20: Initialization and shape optimization for different tests, initialization 2, aluminium, half large cantilever, $V^{\text{target}} = 0.9V^0$

case	$\frac{V}{V^0}$	$C_{\text{ply}}\,(k_g m s^{-2})$	$L_\Gamma\,(m)$	$\overline{C_\phi}$	$\overline{C_{M,\Omega}}$	$\overline{C_{M,D\setminus\Omega}}$
INI	1.00	$2.27e-05$	$1.68e-02$	$5.97e-03$	$0.00e+00$	$8.49e-03$
SONLY	0.90	$9.05e-06$	$1.68e-02$	$2.92e-03$	$0.00e+00$	$2.72e-03$
STEMP	0.90	$9.90e-06$	$1.68e-02$	$2.03e-03$	$0.00e+00$	$8.50e-07$
SP-fromINI	0.90	$8.99e-06$	$3.02e-02$	$8.43e-06$	$0.00e+00$	$1.04e-05$
PONLY	0.90	$9.05e-06$	$2.59e-02$	$2.66e-05$	$0.00e+00$	$1.81e-05$
SP-fromPONLY	0.90	$9.31e-06$	$2.91e-02$	$6.10e-06$	$0.00e+00$	$7.89e-06$

Table 10: Quantitative results for the different tests, initialization 2, aluminium, half large cantilever, $V^{\text{target}} = 0.9V^0$

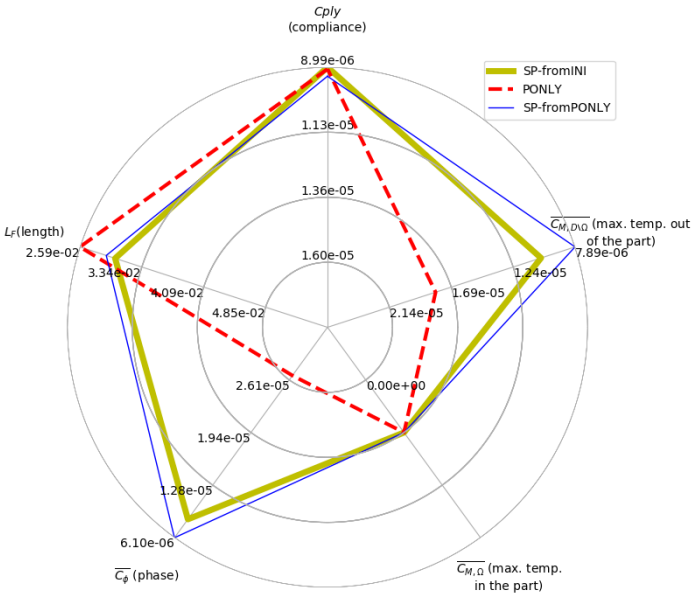

Figure 21: Radar chart of the values given in Table 10 (but for the volume), initialization 2, aluminium, half large cantilever, $V^{\text{target}} = 0.9V^0$

Increasing the size of the working domain can be intuitively understood as a decrease of the conductivity. Indeed, compared to the working domain, the zone melted by the initialization in Figure 18 is thinner than in Figure 8. The path and shape must further adapt. The results obtained for $V^{\text{target}} = 0.9V^0$ lead to similar conclusions than for the results for the titanium in a small working domain (Figures 13 and 15). The bars thickness is once again very important and to cover thick bars, specific patterns appear. In Figure 18, the initialization of the path is composed of straight lines. Yet, it seems that once again Omega-patterns are designed (especially in Figure 18 (d)). The paths resulting from PONLY (Figure 18 (e)) and concurrent optimization starting from the result of PONLY (Figure 18 (f)) still present the Omega-pattern especially in the left lower bar. They also seem to introduce a second pattern referred to as Wave-pattern in the following. The second initialization (Figure 20 (a)) is chosen to widen the melted zone at the initial state. It clearly impacts the results by preventing the creation of these Wave-patterns but still deforming the initial path to introduce once again Omega-patterns. In both cases, it is very clear that the algorithm seems to naturally introduce repetitive patterns which is very interesting for industrial applications and should be further studied. A final observation, a lot clearer in this large domain context than in the classic one, is that adapting the shape improves the results. Completely straightforward in Figure 20 (c) but also in the different concurrent optimizations and especially Figures 18 (f) and 20 (f), the shape boundary fits the melted domain introducing slight oscillations. The damages on the compliance remaining small, this observation confirms the importance of introducing shape constraints to facilitate path designs.

As for $V^{\text{target}} = 1.1V^0$, the results are given by Figure 22, Table 11 and Figure 23 for the first initialization and Figure 24, Table 12 and Figure 25 for the second.

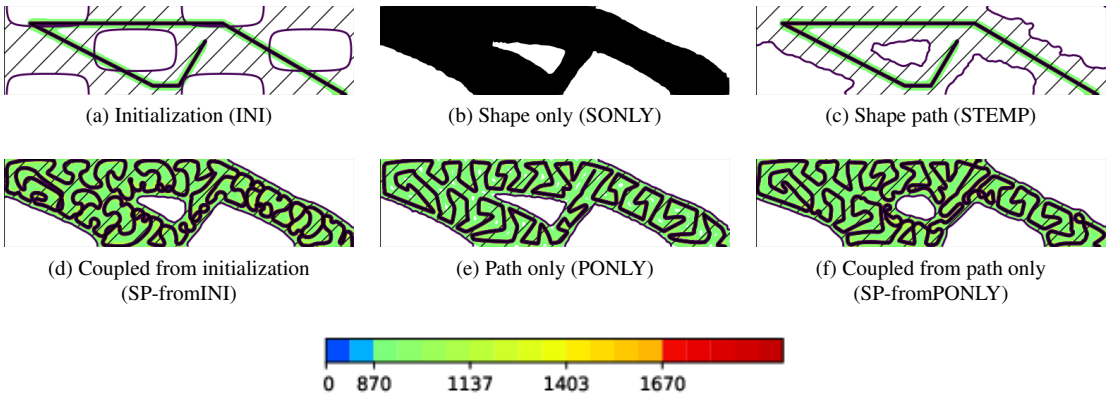

(a) Initialization (INI) (b) Shape only (SONLY) (c) Shape path (STEMP)

(d) Coupled from initialization (SP-fromINI) (e) Path only (PONLY) (f) Coupled from path only (SP-fromPONLY)

(g) Temperature colorbar (K)

Figure 22: Initialization and shape optimization for different tests, initialization 1, aluminium, half large cantilever, $V^{\text{target}} = 1.1V^0$

case	$\frac{V}{V^0}$	$C_{\text{ply}}\,(k_g m s^{-2})$	$L_\Gamma\,(m)$	$\overline{C_\phi}$	$\overline{C_{M,\Omega}}$	$\overline{C_{M,D\setminus\Omega}}$
INI	1.00	$2.27e-05$	$8.77e-03$	$8.07e-03$	$0.00e+00$	$3.54e-03$
SONLY	1.10	$7.67e-06$	$8.77e-03$	$6.74e-03$	$0.00e+00$	$0.00e+00$
STEMP	1.10	$8.03e-06$	$8.77e-03$	$6.68e-03$	$0.00e+00$	$0.00e+00$
SP-fromINI	1.10	$7.69e-06$	$3.84e-02$	$4.41e-06$	$0.00e+00$	$5.16e-06$
PONLY	1.10	$7.67e-06$	$3.11e-02$	$1.38e-05$	$0.00e+00$	$1.10e-05$
SP-fromPONLY	1.10	$7.77e-06$	$3.52e-02$	$4.31e-06$	$0.00e+00$	$4.43e-06$

Table 11: Quantitative results for the different tests, initialization 1, aluminium, half large cantilever, $V^{\text{target}} = 1.1V^0$

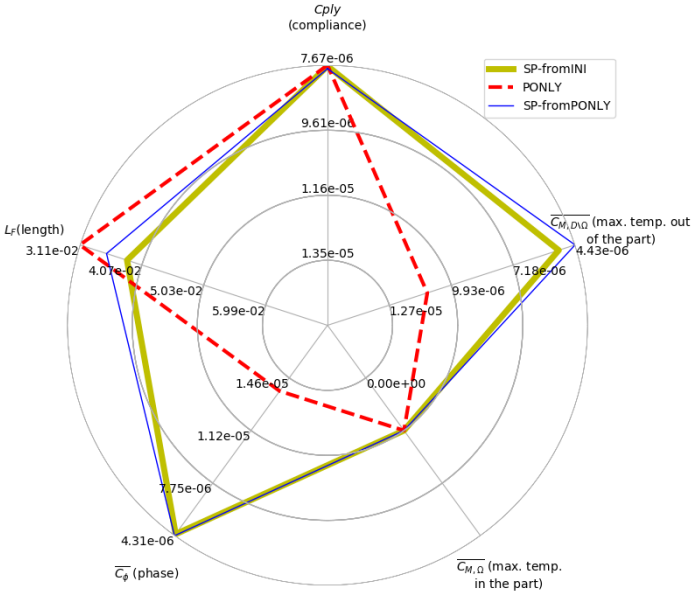

Figure 23: Radar chart of the values given in Table 11 (but for the volume), initialization 1, aluminium, half large cantilever, $V^{\text{target}} = 1.1V^0$

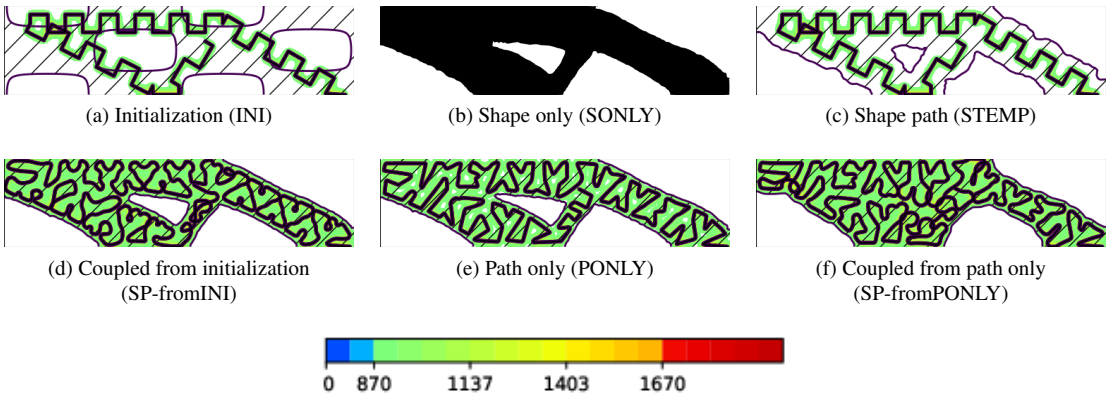

(a) Initialization (INI) (b) Shape only (SONLY) (c) Shape path (STEMP)

(d) Coupled from initialization (SP-fromINI) (e) Path only (PONLY) (f) Coupled from path only (SP-fromPONLY)

(g) Temperature colorbar (K)

Figure 24: Initialization and shape optimization for different tests, initialization 2, aluminium, half large cantilever, $V^{\text{target}} = 1.1V^0$

case	$\frac{V}{V^0}$	$C_{\text{ply}}\,(k_g m s^{-2})$	$L_\Gamma\,(m)$	$\overline{C_\phi}$	$\overline{C_{M,\Omega}}$	$\overline{C_{M,D\setminus\Omega}}$
INI	1.00	$2.27e-05$	$1.68e-02$	$5.97e-03$	$0.00e+00$	$8.49e-03$
SONLY	1.10	$7.67e-06$	$1.68e-02$	$3.64e-03$	$0.00e+00$	$2.90e-04$
STEMP	1.10	$8.05e-06$	$1.68e-02$	$3.42e-03$	$0.00e+00$	$0.00e+00$
SP-fromINI	1.10	$7.67e-06$	$3.56e-02$	$4.71e-06$	$0.00e+00$	$5.74e-06$
PONLY	1.10	$7.67e-06$	$3.09e-02$	$2.35e-05$	$0.00e+00$	$6.29e-06$
SP-fromPONLY	1.10	$8.04e-06$	$3.65e-02$	$2.99e-06$	$0.00e+00$	$3.53e-06$

Table 12: Quantitative results for the different tests, initialization 2, aluminium, half large cantilever, $V^{\text{target}} = 1.1V^0$

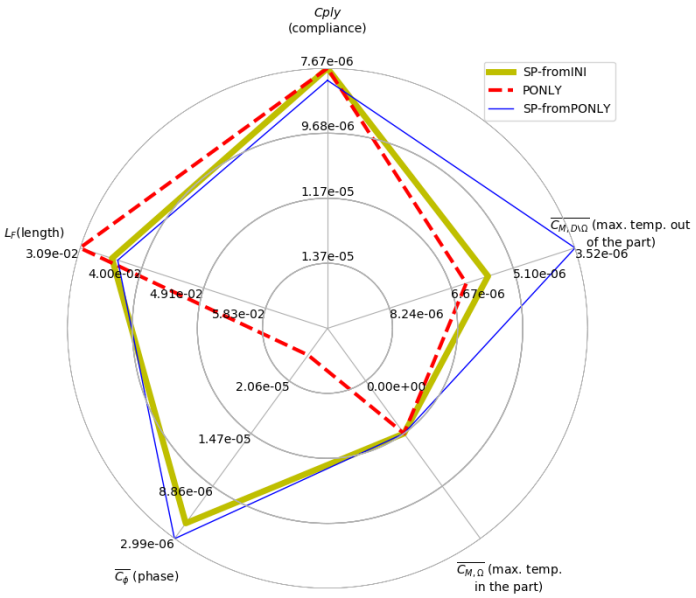

Figure 25: Radar chart of the values given in Table 12 (but for the volume), initialization 2, aluminium, half large cantilever, $V^{\text{target}} = 1.1V^0$

With $V^{\text{target}} = 1.1V^0$, the conclusions are quite similar. Since the bars to melt are larger, the patterns are now closer to the Wave-pattern in Figure 22 (d-e-f). In Figure 24 (d-e-f), the patterns are closer to Omega-pattern, the path initialization chosen impacting strongly these results. It is once again very clear that the shape adapt to the melted zones with the modification of the inner hole size in Figures 22 and 24 (d) and (f) (the hole even disappears in Figure 24 (f)) and with stronger oscillations in the boundary, especially when running concurrent optimization starting from PONLY (Figures 22 and 24 (f)).

5.2.2 Titanium test case

To further complicate the optimization, these tests with a larger domain are now run with the titanium. The Figures presenting the results for $V^{\text{target}} = 0.9V^0$ are given by Figure 26, Table 13 and Figure 27 for the first initialization and Figure 28, Table 14 and Figure 29 for the second initialization. As for the tests for $V^{\text{target}} = 1.1V^0$, they are given by Figure 30, Table 15 and Figure 31 for the first initialization and Figure 32, Table 16 and Figure 33 for the second initialization.

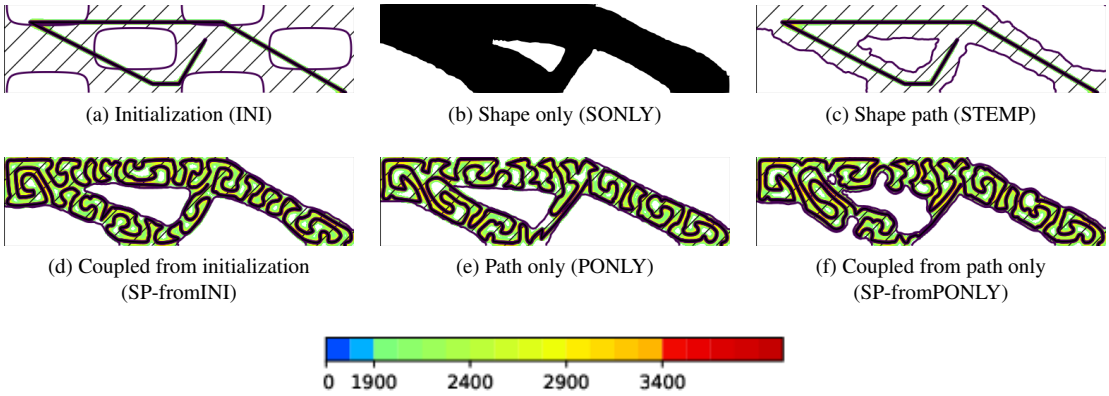

(a) Initialization (INI)
(b) Shape only (SONLY)
(c) Shape path (STEMP)
(d) Coupled from initialization (SP-fromINI)
(e) Path only (PONLY)
(f) Coupled from path only (SP-fromPONLY)
(g) Temperature colorbar (K)

Figure 26: Initialization and shape optimization for different tests, initialization 1, titanium, half large cantilever, $V^{\text{target}} = 0.9V^0$

case	$\frac{V}{V^0}$	$C_{\text{ply}}\,(k_g m s^{-2})$	$L_\Gamma\,(m)$	$\overline{C_\phi}$	$\overline{C_{M,\Omega}}$	$\overline{C_{M,D\setminus\Omega}}$
INI	1.00	$2.27e-05$	$8.77e-03$	$8.07e-03$	$0.00e+00$	$3.54e-03$
SONLY	0.90	$9.05e-06$	$8.77e-03$	$6.01e-03$	$0.00e+00$	$9.19e-04$
STEMP	0.90	$9.44e-06$	$8.77e-03$	$5.45e-03$	$0.00e+00$	$0.00e+00$
SP-fromINI	0.90	$9.01e-06$	$2.99e-02$	$7.07e-06$	$0.00e+00$	$1.20e-05$
PONLY	0.90	$9.05e-06$	$2.63e-02$	$6.02e-05$	$0.00e+00$	$1.28e-04$
SP-fromPONLY	0.90	$9.37e-06$	$2.98e-02$	$5.56e-06$	$0.00e+00$	$7.55e-06$

Table 13: Quantitative results for the different tests, initialization 1, titanium, half large cantilever, $V^{\text{target}} = 0.9V^0$

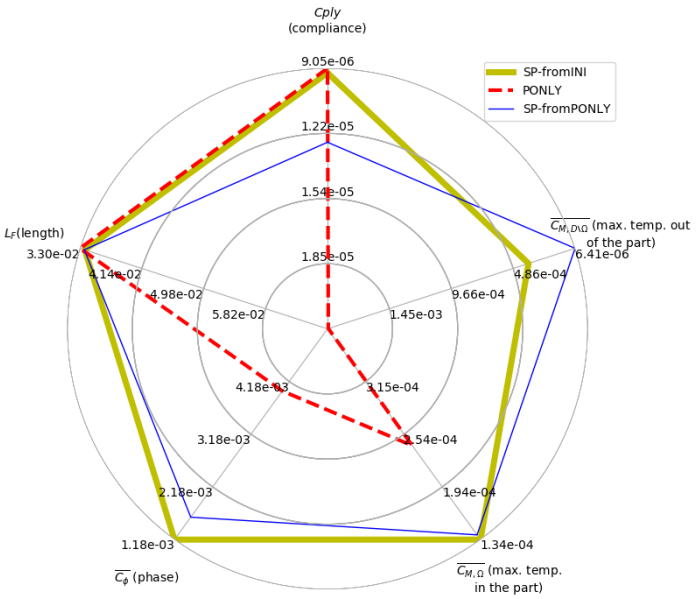

Figure 27: Radar chart of the values given in Table 13 (but for the volume), initialization 1, titanium, half large cantilever, $V^{\text{target}} = 0.9V^0$

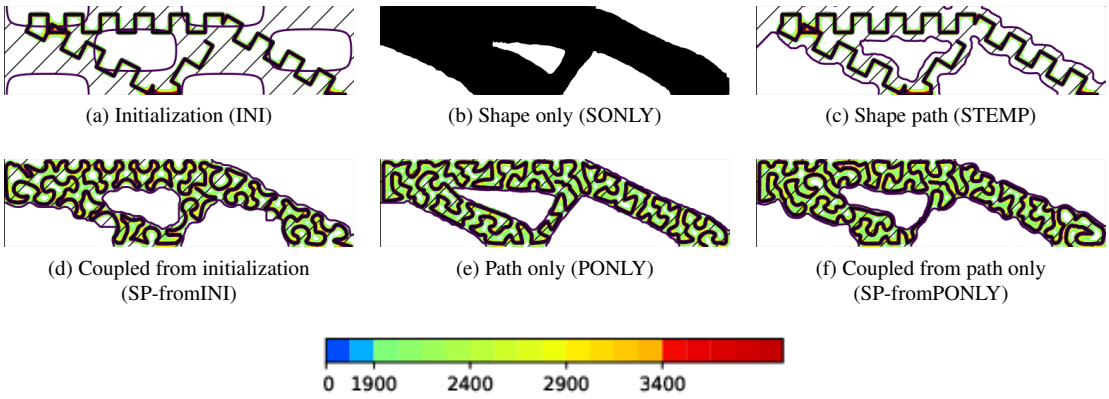

(a) Initialization (INI)
(b) Shape only (SONLY)
(c) Shape path (STEMP)
(d) Coupled from initialization (SP-fromINI)
(e) Path only (PONLY)
(f) Coupled from path only (SP-fromPONLY)
(g) Temperature colorbar (K)

Figure 28: Initialization and shape optimization for different tests, initialization 2, titanium, half large cantilever, $V^{\text{target}} = 0.9V^0$

case	$\frac{V}{V^0}$	$C_{\text{ply}}\,(k_g m s^{-2})$	$L_\Gamma\,(m)$	$\overline{C_\phi}$	$\overline{C_{M,\Omega}}$	$\overline{C_{M,D\setminus\Omega}}$
INI	1.00	$2.27e-05$	$1.68e-02$	$5.97e-03$	$0.00e+00$	$8.49e-03$
SONLY	0.90	$9.05e-06$	$1.68e-02$	$2.92e-03$	$0.00e+00$	$2.72e-03$
STEMP	0.90	$9.90e-06$	$1.68e-02$	$2.03e-03$	$0.00e+00$	$8.50e-07$
SP-fromINI	0.90	$8.99e-06$	$3.02e-02$	$8.43e-06$	$0.00e+00$	$1.04e-05$
PONLY	0.90	$9.05e-06$	$2.59e-02$	$2.66e-05$	$0.00e+00$	$1.81e-05$
SP-fromPONLY	0.90	$9.31e-06$	$2.91e-02$	$6.10e-06$	$0.00e+00$	$7.89e-06$

Table 14: Quantitative results for the different tests, initialization 2, titanium, half large cantilever, $V^{\text{target}} = 0.9V^0$

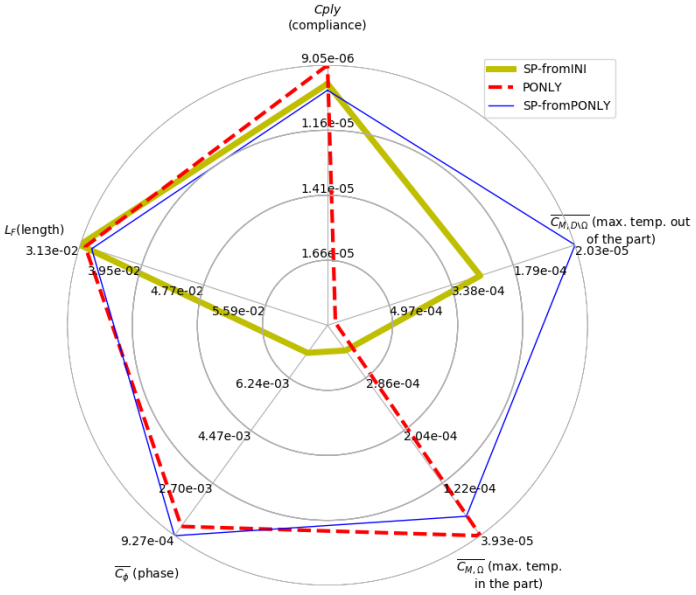

Figure 29: Radar chart of the values given in Table 14 (but for the volume), initialization 2, titanium, half large cantilever, $V^{\text{target}} = 0.9V^0$

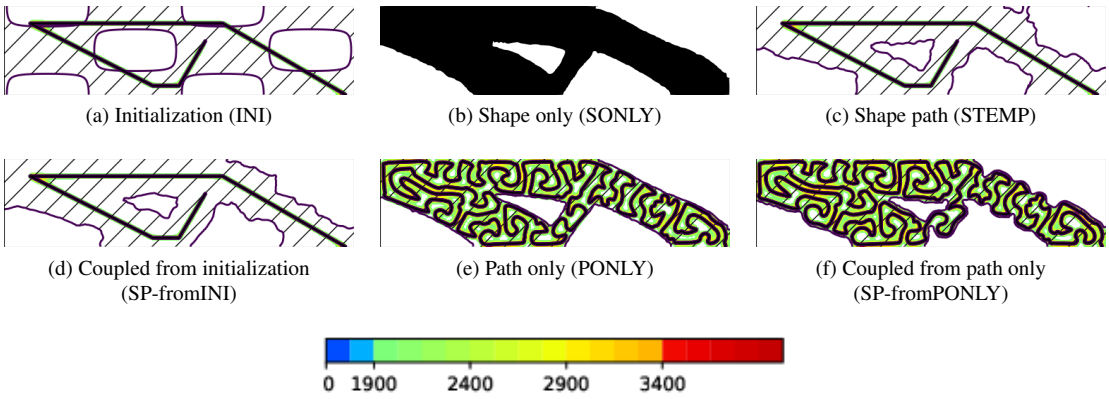

(a) Initialization (INI) (b) Shape only (SONLY) (c) Shape path (STEMP)

(d) Coupled from initialization (SP-fromINI) (e) Path only (PONLY) (f) Coupled from path only (SP-fromPONLY)

(g) Temperature colorbar (K)

Figure 30: Initialization and shape optimization for different tests, initialization 1, titanium, half large cantilever, $V^{\text{target}} = 1.1V^0$

case	$\frac{V}{V^0}$	$C_{\text{ply}}\,(k_g m s^{-2})$	$L_\Gamma\,(m)$	$\overline{C_\phi}$	$\overline{C_{M,\Omega}}$	$\overline{C_{M,D\setminus\Omega}}$
INI	1.00	$2.27e-05$	$8.77e-03$	$8.07e-03$	$0.00e+00$	$3.54e-03$
SONLY	1.10	$7.67e-06$	$8.77e-03$	$6.74e-03$	$0.00e+00$	$0.00e+00$
STEMP	1.10	$8.03e-06$	$8.77e-03$	$6.68e-03$	$0.00e+00$	$0.00e+00$
SP-fromINI	1.10	$7.69e-06$	$3.84e-02$	$4.41e-06$	$0.00e+00$	$5.16e-06$
PONLY	1.10	$7.67e-06$	$3.11e-02$	$1.38e-05$	$0.00e+00$	$1.10e-05$
SP-fromPONLY	1.10	$7.77e-06$	$3.52e-02$	$4.31e-06$	$0.00e+00$	$4.43e-06$

Table 15: Quantitative results for the different tests, initialization 1, titanium, half large cantilever, $V^{\text{target}} = 1.1V^0$

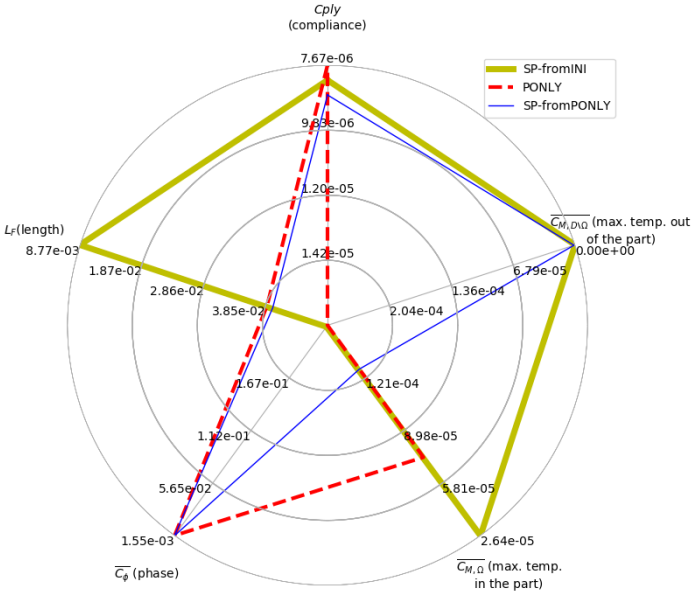

Figure 31: Radar chart of the values given in Table 15 (but for the volume), initialization 1, titanium, half large cantilever, $V^{\text{target}} = 1.1V^0$

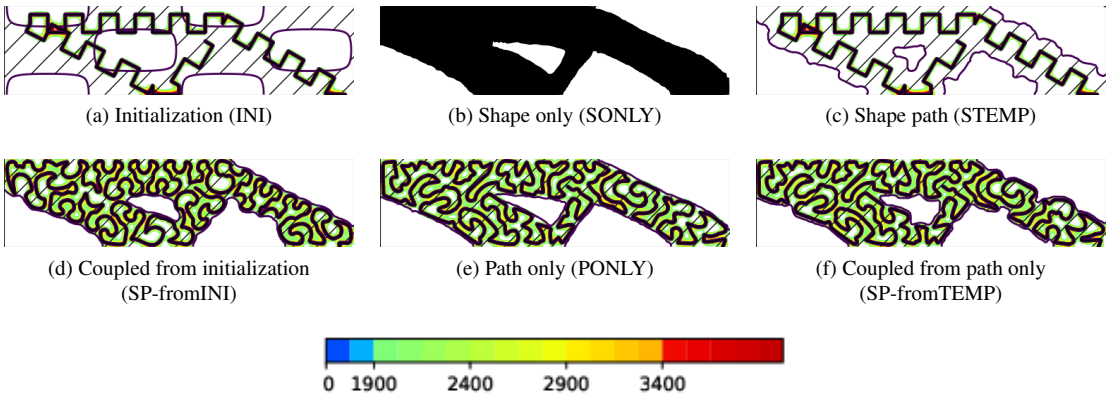

(a) Initialization (INI) (b) Shape only (SONLY) (c) Shape path (STEMP)

(d) Coupled from initialization (SP-fromINI) (e) Path only (PONLY) (f) Coupled from path only (SP-fromTEMP)

(g) Temperature colorbar (K)

Figure 32: Initialization and shape optimization for different tests, initialization 2, titanium, half large cantilever, $V^{\text{target}} = 1.1V^0$

case	$\frac{V}{V^0}$	$C_{\text{ply}}\,(k_g m s^{-2})$	$L_\Gamma\,(m)$	$\overline{C_\phi}$	$\overline{C_{M,\Omega}}$	$\overline{C_{M,D\setminus\Omega}}$
INI	1.00	$2.27e-05$	$1.68e-02$	$5.97e-03$	$0.00e+00$	$8.49e-03$
SONLY	1.10	$7.67e-06$	$1.68e-02$	$3.64e-03$	$0.00e+00$	$2.90e-04$
STEMP	1.10	$8.05e-06$	$1.68e-02$	$3.42e-03$	$0.00e+00$	$0.00e+00$
SP-fromINI	1.10	$7.67e-06$	$3.56e-02$	$4.71e-06$	$0.00e+00$	$5.74e-06$
PONLY	1.10	$7.67e-06$	$3.09e-02$	$2.35e-05$	$0.00e+00$	$6.29e-06$
SP-fromPONLY	1.10	$8.04e-06$	$3.65e-02$	$2.99e-06$	$0.00e+00$	$3.53e-06$

Table 16: Quantitative results for the different tests, initialization 2, titanium, half large cantilever, $V^{\text{target}} = 1.1V^0$

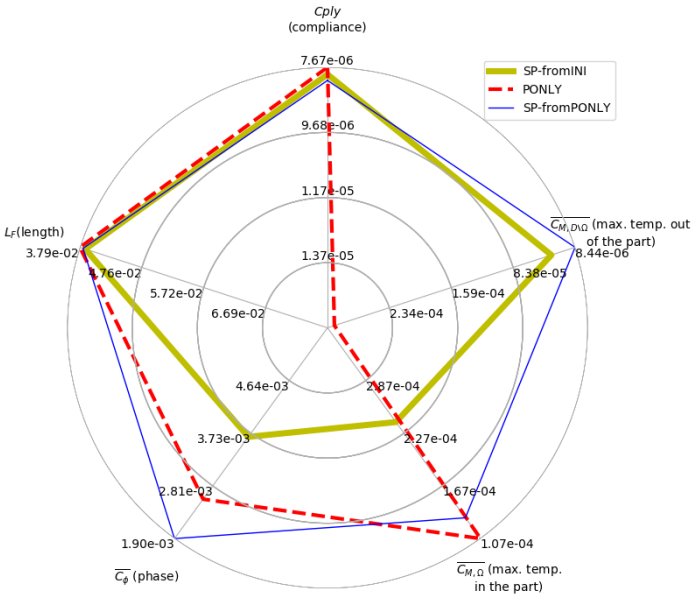

Figure 33: Radar chart of the values given in Table 16 (but for the volume), initialization 2, titanium, half large cantilever, $V^{\text{target}} = 1.1V^0$

In this new test case, filling this higher volume is very hard for the path. The results keep hinting towards a relation between the filling pattern and the thickness of the bar. In Figure 26 (d-e), it seems that thin bars are filled in with a Omega-pattern whereas thicker bars at the upper left corner are filled in with a strong Wave-pattern. On Figure 26 (f), it also seems that the algorithm can take advantage of the low conductivity to build bars that only require a straight line to be melted. Very thin, they still maintain a correct compliance. These observations can be spread to Figures 30. As for zigzag initializations, they lead to slightly different patterns corresponding to a mix between Omega- and Wave-patterns. Yet, the relation between thickness and pattern

happens in these tests too with the presence of Wave-patterns especially in the top left corners of Figures 28 (d-e-f) and 32 (d-e-f). As in the small working domain, the low conductivity of the titanium emphasizes the adaptation of the shape to the temperature. At the cost of compliance, this is very well illustrated by Figure 26 (f) in which the inner hole corresponds to a non intuitive shape fitting the path. If this is less explicit in the other results, the algorithm still created boundary oscillations.

6 Conclusion and perspectives

In this work, the path optimization algorithm developed in [26, 25] has been adapted to handle concurrent optimization of the path and the part's shape and topology in the steady state case. The concurrent algorithm relies on alternate optimization of the shape and topology and the path at each iteration. Yet simple, it has interesting features and yields promising results. The first feature is the importance of the initialization. Already pointed out in [26, 25], the scanning path optimization problem is full of good local minima. In concurrent optimization this issue also influences the part's structure and requires further assessments. It would be especially relevant to work on computationally efficient initialization algorithms. The second and most important feature is the clear relation between scanning path and part's shape and topology: the latter really adapts to the temperature constraints coming from path optimization and can be crucial in their fulfillment. This is well illustrated by the relation between thickness, material properties and scanning parameters: too thin, the bar cannot be accurately built; thicker, it induces an Omega-pattern strategy of the path; even thicker, Wave-pattern arises.
These promising results open up perspectives. First of all, an in-depth study of the impact of the thickness on the scanning path should be conducted. For this purpose, more tests should be run and especially under different mechanical test cases. Then, as mentioned in Section 5, the scanning path optimization itself should be further developed, to allow for path splitting or prevent auto-intersections for example. The model could also be expanded by a mechanical analysis of the residual stresses (inherent strain method for example [30, 31]) and even by including constraints representing the kinematics of the problem (curvature control for example). Such improvements would then allow for three dimensional developments with at least a computation of an optimal solution of successive layers or the adaptation of the steady state algorithm to a transient algorithm. Finally, the results obtained and especially the Omega-pattern and Wave-pattern should be tested on real machines to get experimental information on their relevance and efficiency.

7 Acknowledgments

This work is supported by the SOFIA project, funded by Bpifrance (Banque Publique d'Investissement). We thank Forian Feppon for providing some of his optimization routines.

References

[1] W. Gao, Y. Zhang, D. Ramanujan, K. Ramani, Y. Chen, C.B. Williams, C.C.L. Wang, Y.C. Shin, S. Zhang, and P.D. Zavattieri. The status, challenges, and future of additive manufacturing in engineering. *Computer-Aided Design*, 69:65–89, 2015.

[2] T. DebRoy, H.L. Wei, J.S. Zuback, T. Mukherjee, J.W. Elmer, J.O. Milewski, A.M. Beese, A. Wilson-Heid, A. De, and W. Zhang. Additive manufacturing of metallic components–process, structure and properties. *Progress in Materials Science*, 92:112–224, 2018.

[3] J.O. Milewski. Additive manufacturing of metals. *From Fundamental Technology to Rocket Nozzles, Medical Implants, and Custom Jewelry*, pages 134–157, 2017.

[4] D. Herzog, V. Seyda, E. Wycisk, and C. Emmelmann. Additive manufacturing of metals. *Acta Materialia*, 117:371–392, 2016.

[5] V. Bhavar, P. Kattire, V. Patil, S. Khot, K. Gujar, and R. Singh. A review on powder bed fusion technology of metal additive manufacturing. In *Additive Manufacturing Handbook*, pages 251–253. CRC Press, 2017.

[6] M.K. Thompson, G. Moroni, T. Vaneker, G. Fadel, R.I. Campbell, I. Gibson, A. Bernard, J. Schulz, P. Graf, B. Ahuja, et al. Design for additive manufacturing: Trends, opportunities, considerations, and constraints. *CIRP annals*, 65(2):737–760, 2016.

[7] J.P. Oliveira, A. LaLonde, and J. Ma. Processing parameters in laser powder bed fusion metal additive manufacturing. *Materials & Design*, page 108762, 2020.

[8] M. Megahed, H-W. Mindt, N. N'Dri, H. Duan, and O. Desmaison. Metal additive-manufacturing process and residual stress modeling. *Integrating Materials and Manufacturing Innovation*, 5(1):61–93, 2016.

[9] H-W. Mindt, O. Desmaison, M. Megahed, A. Peralta, and J. Neumann. Modeling of powder bed manufacturing defects. *Journal of Materials Engineering and Performance*, 27(1):32–43, 2018.

[10] P.S. Cook and A.B. Murphy. Simulation of melt pool behaviour during additive manufacturing: Underlying physics and progress. *Additive Manufacturing*, 31:100909, 2020.

[11] H. Shipley, D. McDonnell, M. Culleton, R. Coull, R. Lupoi, G. O'Donnell, and D. Trimble. Optimisation of process parameters to address fundamental challenges during selective laser melting of ti-6al-4v: A review. *International Journal of Machine Tools and Manufacture*, 128:1–20, 2018.

[12] G. Allaire and B. Bogosel. Optimizing supports for additive manufacturing. *Struct. Multidiscip. Optim.*, 58(6):2493–2515, 2018.

[13] G. Allaire, M. Bihr, and B. Bogosel. Support optimization in additive manufacturing for geometric and thermo-mechanical constraints. *Struct. Multidiscip. Optim.*, 61(6):2377–2399, 2020.

[14] J. Liu, A.T. Gaynor, S. Chen, Z. Kang, K. Suresh, A. Takezawa, L. Li, J. Kato, J. Tang, C.C.L. Wang, et al. Current and future trends in topology optimization for additive manufacturing. *Structural and Multidisciplinary Optimization*, 57(6):2457–2483, 2018.

[15] E.M. Arkin, M. Held, and C.L. Smith. Optimization problems related to zigzag pocket machining. *Algorithmica*, 26(2):197–236, 2000.

[16] K. Dai and L. Shaw. Distortion minimization of laser-processed components through control of laser scanning patterns. *Rapid Prototyping Journal*, 8(5):270–276, 2002.

[17] H. Li, Z. Dong, and G.W. Vickers. Optimal toolpath pattern identification for single island, sculptured part rough machining using fuzzy pattern analysis. *Computer-Aided Design*, 26(11):787–795, 1994.

[18] V.T. Rajan, V. Srinivasan, and K.A. Tarabanis. The optimal zigzag direction for filling a two-dimensional region. *Rapid Prototyping Journal*, 7(5):231–241, 2001.

[19] K. Godineau, S. Lavernhe, and C. Tournier. Calibration of galvanometric scan heads for additive manufacturing with machine assembly defects consideration. *Additive Manufacturing*, 26:250–257, 2019.

[20] F. Rasoanarivo, P. Rodriguez-Aycrbe, and D. Dumur. Galvanometer scanner modeling for selective laser melting deflection system simulation. In *2018 15th International Conference on Control, Automation, Robotics and Vision (ICARCV)*, pages 1170–1175. IEEE, 2018.

[21] B. Cheng, S. Shrestha, and K. Chou. Stress and deformation evaluations of scanning strategy effect in selective laser melting. *Additive Manufacturing*, 12:240–251, 2016.

[22] J. Jhabvala, E. Boillat, T. Antignac, and R. Glardon. On the effect of scanning strategies in the selective laser melting process. *Virtual and physical prototyping*, 5(2):99–109, 2010.

[23] L. Ma and H. Bin. Temperature and stress analysis and simulation in fractal scanning-based laser sintering. *The International Journal of Advanced Manufacturing Technology*, 34(9-10):898–903, 2007.

[24] D. Ding, Z. Pan, D. Cuiuri, H. Li, and S. van Duin. Advanced design for additive manufacturing: 3d slicing and 2d path planning. *New trends in 3d printing*, pages 1–23, 2016.

[25] M. Boissier, G. Allaire, and C. Tournier. Scanning path optimization using shape optimization tools. *Structural and Multidisciplinary Optimization*, 61(6):2437–2466, 2020.

[26] M. Boissier. *Coupling structural optimization and trajectory optimization methods in additive manufacturing*. PhD thesis, Institut Polytechnique de Paris, 2020.

[27] T.M. Alam. *Some optimal control problem of partial differential equations and applications to the selective laser melting process (SLM)*. PhD thesis, Université Polytechnique Hauts-de-France, INSA Hauts-De-France, 2020.

[28] T.M. Alam, S. Nicaise, and L. Paquet. An optimal control problem governed by the heat equation with nonconvex constraints applied to the selective laser melting process. *Minimax Theory and its Applications*, 6(2), 2021.

[29] J. Liu and A.C. To. Deposition path planning-integrated structural topology optimization for 3d additive manufacturing subject to self-support constraint. *Computer-Aided Design*, 91:27–45, 2017.

[30] X. Liang, Q. Chen, L. Cheng, D. Hayduke, and A.C. To. Modified inherent strain method for efficient prediction of residual deformation in direct metal laser sintered components. *Computational Mechanics*, 64(6):1719–1733, 2019.

[31] Q. Chen, J. Liu, X. Liang, and A.C. To. A level-set based continuous scanning path optimization method for reducing residual stress and deformation in metal additive manufacturing. *Computer Methods in Applied Mechanics and Engineering*, 360:112719, 2020.

[32] P. Mercelis and J-P. Kruth. Residual stresses in selective laser sintering and selective laser melting. *Rapid prototyping journal*, 12(5):254–265, 2006.

[33] G. Allaire, C. Dapogny, and F. Jouve. Shape and topology optimization. *to appear in Handbook of Numerical Analysis – Geometric PDE's, vol. 2 (preprint hal-02496063)*, 2021.

[34] A. Henrot and M. Pierre. *Shape variation and optimization*. EMS Tracts in Mathematics. European Mathematical Society (EMS), Zürich, 2018.

[35] G. Allaire. *Conception optimale de structures*. Mathématiques & Applications (Berlin) [Mathematics & Applications]. Springer-Verlag, Berlin, 2007.

[36] G. Allaire, F. Jouve, and A-M. Toader. Structural optimization using sensitivity analysis and a level-set method. *J. Comput. Phys.*, 194(1):363–393, 2004.

[37] J. Céa. Conception optimale ou identification de formes: calcul rapide de la dérivée directionnelle de la fonction coût. *RAIRO Modél. Math. Anal. Numér.*, 20, 1986.

[38] B. Mohammadi and O. Pironneau. *Applied shape optimization for fluids*. Oxford university press, 2010.

[39] M. Burger. A framework for the construction of level set methods for shape optimization and reconstruction. *Interfaces Free Bound.*, 5(3):301–329, 2003.

[40] F. de Gournay. Velocity extension for the level-set method and multiple eigenvalues in shape optimization. *SIAM J. Control Optim.*, 45(1):343–367, 2006.

[41] E. Maitre. Review of numerical methods for free interfaces. *Ecole thématique: Modèles de champ de phase pour l' évolution de structures complexes*, 2006.

[42] F. Gibou, R. Fedkiw, and S. Osher. A review of level-set methods and some recent applications. *J. Comput. Phys.*, 353:82–109, 2018.

[43] A. Jafari and N. Ashgriz. Numerical techniques for free surface flows: Interface capturing and interface tracking. *Encyclopedia of Microfluidics and Nanofluidics*, pages 2458–2479, 2015.

[44] S. Osher and R. Fedkiw. *Level set methods and dynamic implicit surfaces*, volume 153 of *Applied Mathematical Sciences*. Springer-Verlag, New York, 2003.

[45] G. Tryggvason, B. Bunner, A. Esmaeeli, D. Juric, N. Al-Rawahi, W. Tauber, J. Han, S. Nas, and Y-J. Jan. A front-tracking method for the computations of multiphase flow. *Journal of computational physics*, 169(2):708–759, 2001.

[46] J. Nocedal and S.J. Wright. *Numerical optimization*. Springer Series in Operations Research and Financial Engineering. Springer, New York, second edition, 2006.

[47] F. Feppon, G. Allaire, and C. Dapogny. Null space gradient flows for constrained optimization with applications to shape optimization. HAL preprint hal-01972915, 2020.

[48] S. Osher and J.A. Sethian. Fronts propagating with curvature-dependent speed: algorithms based on Hamilton-Jacobi formulations. *J. Comput. Phys.*, 79(1):12–49, 1988.

[49] C. Bui, C. Dapogny, and P. Frey. An accurate anisotropic adaptation method for solving the level set advection equation. *Internat. J. Numer. Methods Fluids*, 70(7):899–922, 2012.

[50] C. Dapogny. *Shape optimization, level set methods on unstructured meshes and mesh evolution*. PhD thesis, Université Pierre et Marie Curie, 2013.

[51] ISCD toolbox. Iscdtoolbox: Advection. https://github.com/ISCDtoolbox/Advection.

[52] G. Michailidis. *Manufacturing Constraints and Multi-Phase Shape and Topology Optimization via a Level-Set Method*. PhD thesis, Ecole Polytechnique, 2014.

[53] F. Hecht. New development in FreeFem++. *J. Numer. Math.*, 20(3-4):251–265, 2012.